Journal of Materials Chemistry A

ROYAL SOCIETY OF CHEMISTRY

PAPER

View Article Online
View Journal | View Issue

Cite this: J. Mater. Chem. A, 2024, 12, 2932

Impact of crystal structure on the lattice thermal conductivity of the IV–VI chalcogenides†

Sophie K. Guillemot, [ab] Ady Suwardi, [b] Nikolas Kaltsoyannis [a] and Jonathan M. Skelton *[a]

We present a detailed comparative study of the lattice thermal conductivity κ_{latt} of ten reported phases of the IV–VI chalcogenides GeSe, GeTe, SnSe and SnTe, calculated within the single-mode relaxation-time approximation based on third-order interatomic force constants. Differences in κ_{latt} are attributed quantitatively to the phonon group velocities and lifetimes, and differences in the lifetimes are further attributed to the averaged three-phonon interaction strengths and the "phase space" of allowed energy- and momentum-conserving scattering pathways. Our analysis reveals a complex dependence of the κ_{latt} on the crystal structure: structures that constrain the tetrel atoms to locally-symmetric environments show strong phonon anharmonicity and short lifetimes, but in simple structures such as the rocksalt phase these are counterbalanced by large group velocities and a smaller phase space. We find that these competing effects are optimised for orthorhombic *Cmcm* SnSe, resulting in the lowest predicted κ_{latt} across the ten systems examined. Our findings provide new insight into the interplay between crystal structure and lattice thermal conductivity, and allow us to propose some new guidelines for how to optimise the thermal transport of the IV–VI chalcogenides through crystal engineering.

Received 27th September 2023
Accepted 14th December 2023

DOI: 10.1039/d3ta05885a

rsc.li/materials-a

1 Introduction

In 2015, 196 countries pledged to work together to combat climate change. The Paris Agreements, initiated in 2016, sought to limit the increase in global temperature by the end of this century to 1.5 °C above pre-industrial levels.[1] To meet this goal requires significant changes to how we generate and consume energy: by 2030, 30% of global energy must come from renewable sources, and the efficiency with which energy is used must improve by 32.5%.[2,3] A 2017 report by the International Energy Agency identified key areas of improvement for each of the major signatories to the Paris Agreements, and outlined a "Bridge Scenario" in which improved energy efficiency could account for a 48% reduction in global emissions by 2030.[4] The building, industry and housing sectors alone have the potential to contribute *ca.* 20.7% of this reduction.[4]

While intensive research has led to rapid improvements in primary energy-generation technologies such as photovoltaics and supporting technologies such as batteries and grid-level storage, technologies aimed at enhancing energy efficiency have received less attention. Given that an estimated 60% of the energy used globally is wasted as heat,[5,6] a strong contender in this area are thermoelectric generators (TEGs) to recover waste heat as electrical energy. (The dual function of thermoelectric cooling also has a number of important contemporary applications.[7]) TEGs are solid-state devices with no moving parts, allowing for maintenance-free operation, and have proven reliability in the aerospace industry.[8] They have also been proposed for, among other things, powering wireless sensors, recovering waste heat from household chimneys, and improving the efficiency of combustion engines.[5,9]

The performance of a thermoelectric material is often measured through the dimensionless figure of merit ZT:[10]

$$ZT = \frac{S^2\sigma T}{\kappa_{elec} + \kappa_{latt}} \quad (1)$$

where S is the Seebeck coefficient, σ is the electrical conductivity, $S^2\sigma$ is the power factor (PF), and κ is the thermal conductivity given by the sum of the electronic and lattice (phonon) components κ_{elec} + κ_{latt}. The electronic transport

[a]Department of Chemistry, University of Manchester, Oxford Road, Manchester M13 9PL, UK. E-mail: jonathan.skelton@manchester.ac.uk

[b]Institute of Materials Research and Engineering (IMRE), Agency for Science, Technology and Research (A*STAR), 1 Fusionopolis Way, #20-10 Connexis North Tower, Singapore 138632, Singapore

† Electronic supplementary information (ESI) available: Phonon dispersion and density of states curves of the ten systems examined in this work; anisotropy in the calculated lattice thermal conductivity; comparison of the averaged phonon lifetimes at 300 K to the frequency spectra of the lifetimes; phonon-scattering phase spaces including contributions from collision and decay processes; determination of the averaged three-phonon interaction strengths and comparison to the frequency spectra of the modal interaction strengths; comparison of thermal-conductivity calculations using the single-mode relaxation-time approximation and by direct solution of the linearised phonon Boltzmann transport equation; and comparison of the frequency spectra of the phonon lifetimes at 300 K to the Ioffe–Regel limit in time. See DOI: https://doi.org/10.1039/d3ta05885a

coefficients in eqn (1), *viz.* S, σ, and κ_{elec}, are interrelated through the carrier concentration n such that ZT is generally optimised in the range of $n = 10^{19} - 10^{20}$ cm^{-3} typical of heavily-doped semiconductors.[10] The lattice thermal conductivity κ_{latt}, on the other hand, can in theory be optimised independently, and minimising κ_{latt} is therefore an important avenue of research for improving ZT. While the structure–property relationships that underpin low κ_{latt} are not well understood at present, it is typical of materials with large/complex crystallographic unit cells containing many atoms, made of heavy elements, and/or with weak chemical bonding. Other structural features such as "active" lone pairs and layering are also known to reduce κ_{latt}, by increasing phonon anharmonicity and introducing discontinuities in the bonding network respectively.[11,12]

The IV–VI chalcogenides show a good balance of favourable electrical transport properties and low κ_{latt}, and as such are among the most widely-studied TEs for mid- to high-temperature applications.[13–15] The lead chalcogenides PbS, PbSe and PbTe have been widely studied, and nanostructured PbTe, with a maximum ZT_{max} of 2.2 at 915 K, is a current industry-standard high-temperature TE.[16,17] The high thermoelectric performance of PbTe arises from a low κ_{latt} due to strong phonon anharmonicity and favourable electronic transport due to "band convergence" at elevated temperature.[18,19] Both phenomena are thought to be linked to the high-symmetry cubic rocksalt ($Fm\bar{3}m$) structure adopted by these materials, although the extent of the phonon anharmonicity is disputed.[20–23] However, the toxicity of Pb and the low abundance of Te prevent widespread deployment of PbTe-based TEGs.[24]

Given the high performance of PbTe, SnTe and GeTe have been explored as alternatives. These systems both adopt a rhombohedral ($R3m$) structure, related to the rocksalt structure by a cation off-centering along the [111] direction, below ≈100 and 700 K respectively.[25,26] GeTe shows large intrinsic cation vacancy concentrations, resulting in high carrier concentrations and good electrical conductivity.[15] Co-doping with Group V elements such as Sb, In and Bi, and also alloying with PbTe, has been shown to enhance the electrical properties of GeTe to yield $ZT > 2$.[15,26–28] (We note however that alloying with Pb raises the same issues as the Pb chalcogenides.) Cu- and Mn-doped SnTe also show good thermoelectric performance, with a reported $ZT_{max} = 1.6$ at 925 K.[29] However, a working TEG requires both p- and n-type materials to form a complete device,[17] but to date n-type chalcogenides remain scarce, with one of few examples being $(GeTe)_{1-x}(AgBiSe_2)_x$ with $x > 20\%$.[30,31]

The rarity of Te has also motivated research into the Group IV sulphides and selenides. In particular, SnSe has become one of the benchmark chalcogenide TEs following reports of an unprecedented bulk ZT of 2.6 (ref. 32) and a potential $ZT > 3$ in polycrystalline samples.[28] Unlike the Pb chalcogenides and the tellurides, SnSe adopts an orthorhombic *Pnma* structure at low temperature and transforms to a higher-symmetry orthorhombic *Cmcm* phase on heating. As for PbTe, the record thermoelectric performance of *Cmcm* SnSe[32] has been attributed to a combination of strong phonon anharmonicity, leading to low κ_{latt},[33,34] and a multi-valley band structure that results in favourable electronic transport.[35] The layered structure of SnSe also results in anisotropic transport, such that along the out-of-plane direction the thermal conductivity approaches the amorphous limit while facile electronic transport is retained.[14,28] This effect is somewhat diminished in polycrystalline samples, but is offset by improved mechanical properties.[14] Due to its chemical similarity to SnSe and the isostructural low-temperature *Pnma* phase, GeSe has also seen renewed interest, but the predicted $ZT_{max} \approx 2.5$ has not yet been realised in experiments.[13] This is attributed to the difficulty of forming Ge vacancies leading to a low intrinsic charge-carrier concentration of $n \approx 10^{16}$ cm^{-3}, and the detrimental effect on the power factor is difficult to counteract with single-atom doping due to the low solubility of typical dopants such as Ag and Na in GeSe.[13] GeTe and SnTe are both also reported to undergo a pressure-induced transition to the *Pnma* phase,[28,36,37] and therefore analogous telluride phases may be synthetically accessible.

Given that the high thermoelectric performance of the chalcogenides is due in part to low κ_{latt} attributed to intrinsic phonon anharmonicity, it is of interest to understand the impact of the different crystal structure types adopted across the series on the structural dynamics and thermal transport. First-principles modelling using techniques such as the single-mode relaxation-time approximation (SM-RTA) allows for accurate prediction of the lattice thermal conductivity while providing microscopic detail at the level of individual phonon modes,[38,39] and these calculations have for example played an important role in understanding the low κ_{latt} of SnSe.[33,34] We recently developed a set of techniques for analysing SM-RTA calculations that can be used to attribute differences in κ_{latt} quantitatively to differences in the phonon group velocities and lifetimes, and to quantify the contribution of the strength of the anharmonic phonon interactions to the latter.[40–42] These were recently applied to a family of silicon allotropes and highlighted the important role of structural complexity in determining the κ_{latt}.[42]

In this work, we apply these techniques to investigate the impact of the crystal structure on the lattice thermal conductivity of the Group IV–VI chalcogenides GeSe, GeTe, SnSe and SnTe. We find that the link between the κ_{latt} and different structure types results from a balance of low phonon group velocities, favoured by large primitive cells, and strong phonon anharmonicity and short lifetimes, favoured by structures where the tetrel atoms are constrained to locally symmetric environments. We also find that the shape of the phonon spectra, which determines the so-called "scattering phase space" (the number of allowed energy- and momentum-conserving scattering pathways), also has a prominent influence on the phonon lifetimes. These effects are optimally balanced in the high-temperature *Cmcm* structure of SnSe, which has the lowest κ_{latt} across the ten structures we examine. Our results demonstrate that the crystal structure has a far larger impact on the κ_{latt} than the atomic masses, and the microscopic insight from this analysis provides clear guidelines

for optimising the heat transport in the IV–VI chalcogenides through crystal-structure engineering.

2 Methods

Periodic density-functional theory (DFT) calculations were performed using the Vienna *Ab initio* Simulation Package (VASP) code.[43] Initial structures were obtained from the Materials Project Database[44] or taken from previous work.[33] The PBEsol generalised-gradient approximation (GGA) functional was used to describe electron exchange and correlation.[45] A Hubbard U correction of $U_{\text{eff}} = 4$ eV was applied to the Sn d electrons using the method of Dudarev *et al.*[46] The valence Kohn–Sham orbitals were modelled using plane-wave basis sets with kinetic-energy cutoffs of 400–500 eV (Table 1). The electronic Brillouin zones were integrated using the Γ-centered Monkhorst–Pack $\boldsymbol{k}$-point meshes shown in Table 1. Both parameters were chosen by explicit testing to converge the total energies to <1 meV atom^{-1} and the external pressure to <1 kbar (0.1 GPa). Projector augmented-wave (PAW) pseudopotentials[47,48] were used to model the ion cores, with valence configurations of: Se – $4s^24p^4$; Te – $5s^25p^4$; Ge – $3d^{10}4s^24p^2$; and Sn – $4d^{10}5s^25p^2$. Each of the structures were fully optimised to tolerances of 10^{-8} eV and 10^{-2} eV Å^{-1} on the electronic total energy and atomic forces respectively. The PAW projections were performed in real space, and the precision of the charge density grids was set automatically to avoid aliasing errors.

Lattice-dynamics and thermal-conductivity calculations were set up and post-processed using the Phonopy and Phono3py codes.[39,49] The second and third-order force constants $\boldsymbol{\Phi}^{(2)}/\boldsymbol{\Phi}^{(3)}$ were determined using the supercell finite-difference approach with the supercell expansions and reduced $\boldsymbol{k}$-point sampling listed in Table 1 and displacement step sizes of 10^{-2} and 3×10^{-2} Å respectively. Phonon density of states (DoS) and atom-projected DoS (PDoS) curves $g(\nu)$ were computed by interpolating frequencies onto uniform Γ-centered grids with $24 \times 24 \times 24$ (DoS) and $16 \times 16 \times 16$ subdivisions (PDoS) with a Gaussian smearing of width $\sigma = 0.032$ THz. Phonon dispersion curves $\nu_j(\boldsymbol{q})$ were computed by interpolating the frequencies along strings of $\boldsymbol{q}$-points passing through the high-symmetry wavevectors of the respective Brillouin zones. Where required, transformation matrices were applied to convert the structures and force constants in the conventional cells to the primitive cells for the dispersion calculations. The lattice thermal conductivities were computed using the single-mode relaxation-time approximation (SM-RTA) from modal properties calculated on the Γ-centered $\boldsymbol{q}$-point grids listed in Table 1. We also calculated the κ_{latt} from the full solution of the linearised phonon Boltzmann transport equation (LBTE). The calculated $\boldsymbol{\kappa}_{\text{latt}}$ from the SM-RTA were analysed using the procedures outlined in our previous work.[40–42]

3 Results and discussion

3.1 Chalcogenide phases and optimised structures

We examine ten Group IV–VI chalcogenide systems spanning four compositions, *viz.* GeSe, GeTe, SnSe and SnTe, and four structure types, *viz.* the cubic $Fm\bar{3}m$, rhombohedral $R3m$ and orthorhombic *Pnma* and *Cmcm* structures.

Representative images of the four structure types are shown in Fig. 1. GeSe adopts the disordered orthorhombic *Pnma* structure at low temperature but undergoes a transition to the highly-symmetric $Fm\bar{3}m$ (rocksalt) structure at $T \approx 920$ K.[50,51] GeTe adopts the rhombohedral $R3m$ phase below 690 K and transitions to the $Fm\bar{3}m$ phase above this temperature.[27] The *Pnma* phase of GeTe is also reported to be accessible under applied pressures in the range of 15–37 GPa.[37,52] SnTe behaves similarly to GeTe but the transition from the rhombohedral to the cubic phase occurs below 100 K.[28] A bulk orthorhombic phase is also reported to be accessible under pressure, and has been observed as nanoscale defects in cubic SnTe under ambient conditions.[28] Finally, SnSe adopts the *Pnma* phase at low temperature but undergoes a phase transition to the higher-symmetry orthorhombic *Cmcm* phase around 750 K,[53,54] the latter of which has been shown to display strong phonon

Table 1 List of chalcogenide phases examined in this work with the number of atoms in the primitive (conventional) unit cells and the technical parameters used in the calculations: plane-wave cutoffs and $\boldsymbol{k}$-point sampling meshes used for optimising the unit cells, supercell expansions and reduced $\boldsymbol{k}$-point sampling used to determine the second- and third-order force constants $\boldsymbol{\Phi}^{(2)}/\boldsymbol{\Phi}^{(3)}$ (FCs), and $\boldsymbol{q}$-point sampling used to determine the lattice thermal conductivities $\boldsymbol{\kappa}_{\text{latt}}$. All parameters are based on the conventional unit cells

				2nd-order FCs $\boldsymbol{\Phi}^{(2)}$		3rd-order FCs $\boldsymbol{\Phi}^{(3)}$		
	# atoms	Cutoff [eV]	$\boldsymbol{k}$-points	Supercell (# atoms)	$\boldsymbol{k}$-points	Supercell (# atoms)	$\boldsymbol{k}$-points	$\boldsymbol{\kappa}_{\text{latt}}$ $\boldsymbol{q}$-points
GeSe (*Pnma*)	8 (8)	500	$3 \times 9 \times 7$	$2 \times 4 \times 4$ (256)	$2 \times 3 \times 2$	$1 \times 3 \times 3$ (72)	$3 \times 3 \times 3$	$10 \times 10 \times 10$
GeSe ($Fm\bar{3}m$)	2 (8)	500	$5 \times 5 \times 5$	$3 \times 3 \times 3$ (216)	$2 \times 2 \times 2$	$2 \times 2 \times 2$ (64)	$3 \times 3 \times 3$	$15 \times 15 \times 15$
SnSe (*Pnma*)	8 (8)	450	$3 \times 9 \times 8$	$2 \times 4 \times 4$ (256)	$2 \times 3 \times 2$	$1 \times 3 \times 3$ (72)	$3 \times 3 \times 3$	$9 \times 9 \times 9$
SnSe (*Cmcm*)	4 (8)	450	$8 \times 3 \times 9$	$4 \times 2 \times 4$ (256)	$2 \times 2 \times 3$	$3 \times 1 \times 3$ (72)	$3 \times 3 \times 3$	$12 \times 12 \times 12$
GeTe (*Pnma*)	8 (8)	500	$3 \times 9 \times 8$	$2 \times 4 \times 4$ (256)	$2 \times 3 \times 2$	$1 \times 3 \times 3$ (72)	$3 \times 3 \times 3$	$10 \times 10 \times 10$
GeTe ($R3m$)	2 (6)	500	$8 \times 8 \times 2$	$6 \times 6 \times 2$ (432)	$2 \times 2 \times 2$	$3 \times 3 \times 1$ (54)	$3 \times 3 \times 2$	$12 \times 12 \times 12$
GeTe ($Fm\bar{3}m$)	2 (8)	500	$5 \times 5 \times 5$	$3 \times 3 \times 3$ (216)	$2 \times 2 \times 2$	$2 \times 2 \times 2$ (64)	$3 \times 3 \times 3$	$15 \times 15 \times 15$
SnTe (*Pnma*)	8 (8)	400	$3 \times 10 \times 9$	$2 \times 4 \times 4$ (256)	$2 \times 3 \times 3$	$1 \times 3 \times 3$ (72)	$3 \times 3 \times 3$	$9 \times 9 \times 9$
SnTe ($R3m$)	2 (6)	450	$12 \times 12 \times 4$	$6 \times 6 \times 2$ (432)	$2 \times 2 \times 2$	$3 \times 3 \times 1$ (54)	$3 \times 3 \times 2$	$11 \times 11 \times 11$
SnTe ($Fm\bar{3}m$)	8 (8)	400	$6 \times 6 \times 6$	$3 \times 3 \times 3$ (216)	$2 \times 2 \times 2$	$2 \times 2 \times 2$ (64)	$3 \times 3 \times 3$	$10 \times 10 \times 10$

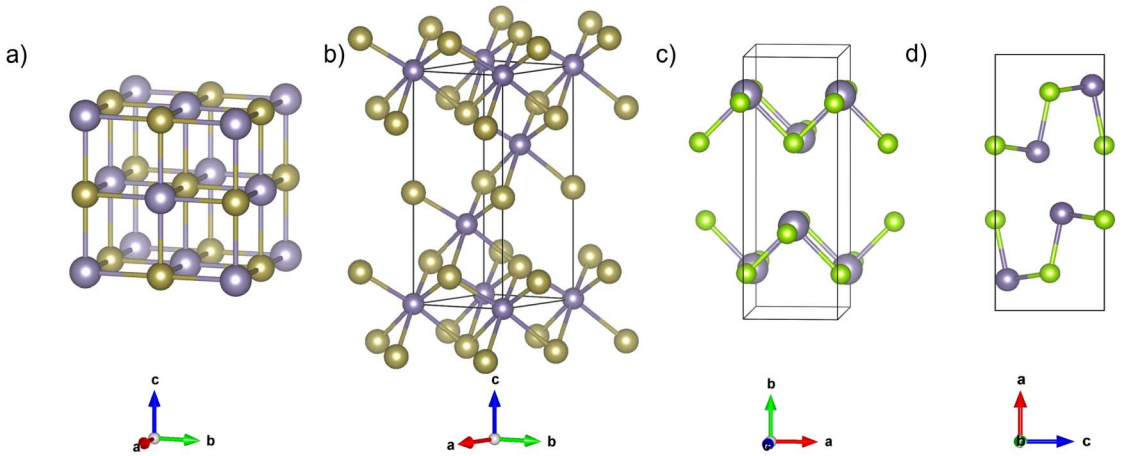

Fig. 1 Representative structures showing the four chalcogenide phases examined in this work: (a) *Fm*$\bar{3}$*m* SnTe; (b) *R*3*m* GeTe; (c) *Cmcm* SnSe; and (d) *Pnma* GeSe. All four structures are shown in the conventional unit cells. The tetrel atoms are shown in grey and the Te and Se atoms are shown in gold and green, respectively. These images were generated using the VESTA software.[56]

Table 2 Optimised lattice parameters of the ten structures examined in this work. The percentage differences to literature values where available are shown in parentheses.[27,36,50,51,53,54,57–59] We also show for each composition the average formula mass $\bar{m}$ and mass difference Δm

					m [amu]	
	a [Å]	b [Å]	c [Å]	V [Å^3]	$\bar{m}$	Δm
GeSe (*Pnma*)	10.79 (−0.4)	3.85 (+0.4)	4.44 (−1.4)	180.6 (−1.1)	75.8	6.34
GeSe (*Fm*$\bar{3}$*m*)	5.54 (−3.4)	5.54 (−3.4)	5.54 (−3.4)	169.9 (−9.7)		
SnSe (*Pnma*)	11.35 (−1.3)	4.12 (−0.7)	4.34 (−2.5)	203.0 (−4.4)	98.8	39.74
SnSe (*Cmcm*)	4.15 (−3.4)	11.35 (−3.1)	4.12 (−4.5)	194.3 (−10.6)		
GeTe (*Pnma*)	11.52 (−2.1)	4.17 (+0.4)	4.45 (+2.1)	213.7 (+0.4)	100.1	54.97
GeTe (*R*3*m*)	4.15 (−0.6)	4.15 (−0.6)	10.41 (−2.6)	155.1 (−4.0)		
GeTe (*Fm*$\bar{3}$*m*)	5.87 (−2.5)	5.87 (−2.5)	5.87 (−2.5)	202.3 (−7.3)		
SnTe (*Pnma*)	11.86 (+2.3)	4.34 (−0.7)	4.51 (+0.7)	232.3 (+2.4)	123.2	8.89
SnTe (*Fm*$\bar{3}$*m*)	6.25 (−1.0)	6.25 (−1.0)	6.25 (−1.0)	244.4 (−3.5)		
SnTe (*R*3*m*)	4.38	4.38	10.84	180.1		

anharmonicity thought to contribute to its exceptional thermoelectric performance.[34,55]

The optimised lattice parameters of each of the ten structures are shown in Table 2. The parameters of all the low-temperature phases are within 5% of literature values.[27,36,50,51,53,54,57–59] Larger errors are obtained for the high-temperature phases, with the calculations predicting an 11% reduction in the cell volume of *Cmcm* SnSe. This is expected given that standard DFT optimisations yield the athermal equilibrium structures, and we therefore attribute the larger % differences for the high-temperature structures to a larger degree of thermal expansion in the measurements.[60]

3.2 Harmonic phonon spectra

Representative phonon spectra of the four structure types are shown in Fig. 2 arranged by decreasing symmetry from *Fm*$\bar{3}$*m* → *R*3*m* → *Cmcm* → *Pnma*. Phonon dispersion and DoS curves for all ten systems are provided in Section 1 of the ESI.†

The number of atoms n_a in the primitive cells increases with decreasing symmetry (*c.f.* Table 1), which results in the number of bands at each wavevector $\boldsymbol{q}$ increasing from $3n_a = 6$ in the *Fm*$\bar{3}$*m* systems to $3n_a = 24$ in the *Pnma* structures. Comparison of the phonon spectra of the *Fm*$\bar{3}$*m* and *R*3*m* structures in Fig. 2a and b, which both have six branches in the dispersion, shows that the symmetry lowering due to the rhombohedral distortion leads to lower degeneracy among the phonon bands. Similarly, the spectra of the orthorhombic *Cmcm* and *Pnma* structures in Fig. 2c and d show more fine structure due to having 12 and 24 branches in the dispersion, respectively.

In *Fm*$\bar{3}$*m* SnTe and *Cmcm* SnSe, the PDoS curves show that the lower and upper-frequency bands are dominated by the tetrel and chalcogen atoms, respectively (Fig. 2a and c). On the other hand, this is not the case for *R*3*m* GeTe and *Pnma* GeSe, for which both atoms make similar contributions across the full frequency spectrum (Fig. 2b and d). Considering the mass differences in Table 2, this behaviour cannot be put down to the

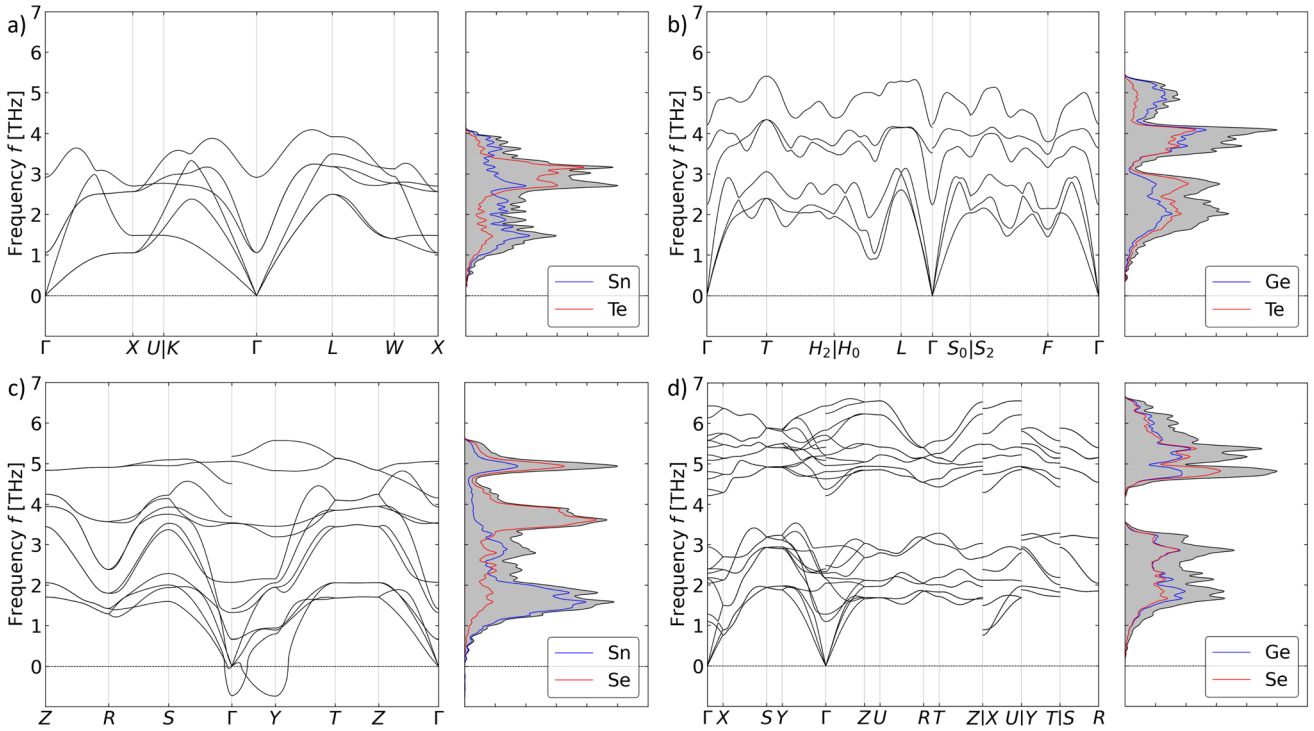

Fig. 2 Representative phonon dispersion and density of states (DoS) curves for the four distinct chalcogenide phases examined in this work: (a) $Fm\bar{3}m$ SnTe; (b) $R3m$ GeTe; (c) *Cmcm* SnSe; and (d) *Pnma* GeSe. On each DoS plot the total DoS is shown as a shaded grey curve and the projections onto the tetrel and chalcogen atoms are shown respectively as blue and red lines.

difference in atomic masses of the tetrel and chalcogen, and instead indicates a difference in the bonding in the Ge and Sn systems. Indeed, the relative contributions of the tetrel and chalcogen atoms to the phonon spectra appear to depend on both the composition and the crystal symmetry. All three $Fm\bar{3}m$ structures show some level of split contributions, which are most prominent in GeSe. $R3m$ GeTe shows roughly equal contributions from both elements across the frequency spectrum, whereas the spectrum of $R3m$ SnTe shows unequal contributions that are particularly prominent in a feature between ~2.5–3.5 THz. With the exception of SnSe, the *Pnma* phases also show roughly equal contributions from the tetrel and chalcogen atoms across the full phonon spectrum, whereas tin selenide shows larger contributions from Sn at low frequencies and larger contributions from Se at higher frequencies. This is also evident in the phonon spectrum of *Cmcm* SnSe. The lower coordination number and more directional bonding in the orthorhombic *Pnma* and *Cmcm* phases may indicate a higher degree of covalent character compared to the higher-symmetry $Fm\bar{3}m$ and $R3m$ phases, which could partially explain differences in the atomic contributions to the phonon spectra. However, to confirm this, or otherwise, would require a more detailed analysis of the chemical bonding, and the different contributions of the tetrel and chalcogen atoms to the lower- and higher-frequency parts of the spectra of the two orthorhombic phases of SnSe suggests there are some deeper subtleties.

The dispersion of *Pnma* GeSe also displays a prominent "band gap" from ~3.5–4 THz (Fig. 2d). This appears to be a feature of the *Pnma* structure, and is most prominent in GeSe and GeTe but also evident in SnSe and SnTe. In the case of SnSe, the gap marks the point where the relative contributions of the tetrel and chalcogen atoms reverse. The spectrum of $R3m$ GeTe also shows a notable reduction in the DoS at mid frequencies, but this is not seen in the spectrum of $R3m$ SnTe, suggesting that the nature of the tetrel atom plays a role in the gap in this structure type. The absence/lower density of modes in the gap range implies that there is no/little contribution to the lattice thermal conductivity at these frequencies, a point to which we return below.

The range of the frequency spectra closely track the average masses. The phonon frequencies in $Fm\bar{3}m$ SnTe, which has the largest average mass of the four systems for which phonon spectra are shown in Fig. 2, range up to ~4 THz, whereas the frequencies in *Pnma* GeSe, which has the smallest average mass, range up to ~7 THz. The frequencies in *Cmcm* SnSe and $R3m$ GeTe, which have similar average masses, both range up to around 6 THz, *i.e.* intermediate between the limits set by SnTe and GeSe. This pattern is observed across all ten systems, regardless of structure type. The "compression" of the phonon spectrum with increasing average mass would be expected to increase the density of allowed phonon scattering pathways at a given frequency, *i.e.* the scattering phase space, which we again investigate further below.

Finally, the spectrum of *Cmcm* SnSe in Fig. 2c shows two imaginary phonon modes at the $\boldsymbol{q} = \Gamma$ and Y wavevectors. These modes are linked to the soft-mode phase transition to the *Pnma* phase.[34] Mapping the instability as a function of the distortion amplitudes Q_Γ and Q_Y (Fig. 3) shows that the *Cmcm*

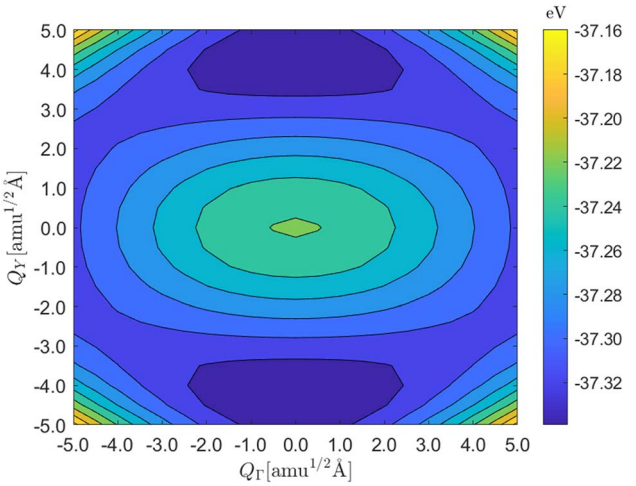

Fig. 3 Two-dimensional structural potential energy surface (PES) spanned by the principal imaginary harmonic modes at the $\boldsymbol{q} = \Gamma$ and $\boldsymbol{q} = Y$ wavevectors in *Cmcm* SnSe as a function of the distortion amplitudes Q_Γ and Q_Y. The *Cmcm* structure is a local maximum, corresponding to a hilltop feature, centred around (0, 0), and connects two equivalent lower-symmetry *Pnma* minima, identified as dark blue, *via* the *Y*-point imaginary mode.

phase is a local maximum on the two-dimensional potential-energy surface (PES) spanned by the principal imaginary modes, connecting two minima located along $\boldsymbol{q} = Y$. These minima correspond to two equivalent distortions of the *Cmcm* structure to the lower-symmetry *Pnma* phase, and the *Cmcm* phase is therefore a "hilltop" on the structural PES connecting *Pnma* minima. The minima are relatively shallow with respect to the hilltop at $(Q_\Gamma = 0, Q_Y = 0)$, and at temperatures above the phase transition the two minima can interconvert sufficiently quickly that experimental techniques that probe the long-range structure (*e.g.* X-ray diffraction) will effectively "see" the *Cmcm* phase as an average structure.[61] On the other hand, *Pnma* SnSe, and indeed all four of the *Pnma* structures examined here, are dynamically stable and do not have imaginary harmonic modes in the dispersion. The soft-mode transition in *Cmcm* SnSe, and its impact on the structure and lattice dynamics, has been the subject of a number of previous studies.[33,34,60,62]

We also note that the spectrum of GeSe has a triply-degenerate imaginary optic mode at the $\boldsymbol{q} = \Gamma$ wavevector, which becomes doubly-degenerate when a non-analytical correction is applied, and this likely indicates a distortion to the *R*3*m* phase. However, we did not pursue this further.

3.3 Lattice thermal conductivity

Within the single-mode relaxation time approximation (SM-RTA) the macroscopic $\boldsymbol{\kappa}_{\text{latt}}$, hereafter $\boldsymbol{\kappa}$, is determined as a sum over microscopic contributions $\boldsymbol{\kappa}_\lambda$ from individual phonon modes $\lambda = \boldsymbol{q}j$ according to:

$$\boldsymbol{\kappa}(T) = \frac{1}{NV}\sum_\lambda \boldsymbol{\kappa}_\lambda(T) = \frac{1}{N_{\boldsymbol{q}}V}\sum_\lambda C_\lambda(T)\boldsymbol{\nu}_\lambda \otimes \boldsymbol{\nu}_\lambda \tau_\lambda(T) \quad (2)$$

The sum is normalised by the unit-cell volume V and the number of wavevectors $N_{\boldsymbol{q}}$ included in the summation. The C_λ are the modal heat capacities given by:

$$C_\lambda(T) = k_{\text{B}} \frac{1}{n_\lambda{}^2(T)} \left(\frac{\hbar\omega_\lambda}{k_{\text{B}}T}\right)^2 \exp(\hbar\omega_\lambda / k_{\text{B}}T) \quad (3)$$

where the ω_λ are the (angular) phonon frequencies and the n_λ are the phonon occupation numbers given by the Bose–Einstein distribution:

$$n_\lambda(T) = \frac{1}{\exp(\hbar\omega_\lambda / k_{\text{B}}T) - 1} \quad (4)$$

The $\boldsymbol{\nu}_\lambda$ are the phonon group velocities given by the derivatives of the ω_λ with respect to $\boldsymbol{q}$, *i.e.* the gradient of the phonon dispersion:

$$\boldsymbol{\nu}_\lambda = \frac{\partial\omega_\lambda}{\partial \boldsymbol{q}} \quad (5)$$

Finally, the τ_λ are the phonon lifetimes calculated from the reciprocal of the phonon linewidths Γ_λ:

$$\tau_\lambda(T) = \frac{1}{\Gamma_\lambda(T)} \quad (6)$$

We discuss further the calculation of the Γ_λ within the SM-RTA in the following subsections.

Fig. 4 compares the calculated $\boldsymbol{\kappa}$ of the ten systems as a function of temperature, and values at $T = 300$ K are summarised in Table 3. For ease of comparison we discuss here the isotropic scalar average κ_{iso} defined as:

$$\kappa_{\text{iso}} = \frac{1}{3}\text{Tr}[\boldsymbol{\kappa}] = \frac{1}{3}(\kappa_{xx} + \kappa_{yy} + \kappa_{zz}) \quad (7)$$

where $\kappa_{\alpha\alpha}$ are the diagonal elements of the $\boldsymbol{\kappa}$ tensor and correspond to transport along the principal x, y and z Cartesian directions. However, the thermal conductivity is only isotropic (*i.e.* all three diagonal components are equal) for the $Fm\bar{3}m$ phase, whereas for the *R*3*m* phase $\kappa_{xx} = \kappa_{yy} \neq \kappa_{zz}$ and for the

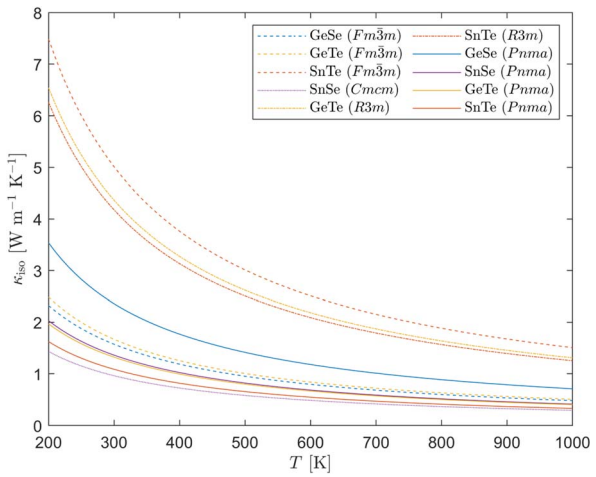

Fig. 4 Calculated scalar-average lattice thermal conductivity κ_{iso} (eqn (7)) as a function of temperature for the ten systems examined in this work.

Table 3 Analysis of the lattice thermal conductivity of the ten compounds examined in this work at $T = 300$ K. For each compound we show the three diagonal components of the $\boldsymbol{\kappa}$ tensor, κ_{xx}, κ_{yy} and κ_{zz}, and the isotropic average κ_{iso} defined in eqn (7), together with the harmonic function $(\boldsymbol{\kappa}/\tau^{CRTA})_{iso}$ and averaged lifetime τ^{CRTA} defined in eqn (9). We also show the integrals of the $\bar{N}_2$ defined in eqn (13) from 0 to the maximum frequencies f_{max} in the phonon spectra, and the averaged phonon–phonon interaction strength $\tilde{P}$ and number of scattering channels $\tilde{N}_2$ defined in eqn (12)–(17)

	$\boldsymbol{\kappa}$ [W m^{-1} K^{-1}]				$(\boldsymbol{\kappa}/\tau^{CRTA})_{iso}$	τ^{CRTA}	$\int_0^{f_{max}} \frac{\bar{N}_2(f)}{(3n_a)^2} df$	$\tilde{P} \times (3n_a)^2$	$\tilde{N}_2/(3n_a)^2$
	κ_{xx}	κ_{yy}	κ_{zz}	κ_{iso}	[W m^{-1} K^{-1} ps^{-1}]	[ps]		[eV^2]	[THz^{-1}]
SnSe (*Cmcm*)	0.39	0.79	1.18	0.96	1.09	0.88	1.36	1.46×10^{-7}	4.74×10^{-3}
SnTe (*Pnma*)	0.63	1.41	1.23	1.09	0.27	3.98	6.22	9.02×10^{-9}	1.70×10^{-2}
GeTe (*Pnma*)	0.45	2.09	1.43	1.32	0.34	3.91	5.39	1.35×10^{-8}	1.15×10^{-2}
SnSe (*Pnma*)	0.91	1.83	1.34	1.36	0.35	3.89	5.22	1.20×10^{-8}	1.31×10^{-2}
GeSe (*Fm*$\bar{3}$*m*)	1.57	—	—	1.57	3.29	0.48	0.28	2.24×10^{-6}	5.69×10^{-4}
GeTe (*Fm*$\bar{3}$*m*)	1.67	—	—	1.67	2.99	0.56	0.33	1.31×10^{-6}	8.35×10^{-4}
GeSe (*Pnma*)	1.05	3.93	2.09	2.36	0.39	6.03	4.39	1.36×10^{-8}	7.44×10^{-3}
SnTe (*R*3*m*)	4.27	—	3.99	4.18	0.69	6.07	0.63	5.20×10^{-8}	1.93×10^{-3}
GeTe (*R*3*m*)	4.71	—	3.67	4.36	0.87	5.01	0.53	8.97×10^{-8}	1.36×10^{-3}
SnTe (*Fm*$\bar{3}$*m*)	5.01	—	—	5.01	1.07	4.67	0.37	1.09×10^{-7}	1.20×10^{-3}

orthorhombic *Pnma* and *Cmcm* phases $\kappa_{xx} \neq \kappa_{yy} \neq \kappa_{zz}$. For each compound, we show the separate temperature dependencies of the κ_{xx}, κ_{yy} and κ_{zz} in Section 2 of the ESI† and the values at 300 K are included in Table 3.

The 300 K $\kappa_{iso} = 1.36$ W m^{-1} K^{-1} calculated for *Pnma* SnSe is comparable to our previous calculations of 1.28 and 1.58 W m^{-1} K^{-1}, and to the higher range of the experimental measurements of 0.7–1.4 and 0.5–0.9 W m^{-1} K^{-1} along the in-plane and layering directions.[32,33,41] We attribute the differences to previous calculations primarily to the different supercell used for the force-constant calculations compared to ref. 33 and to the omission of a dispersion correction compared to ref. 41. Our previous calculations on *Cmcm* SnSe yielded a κ_{iso} of 0.33 W m^{-1} K^{-1} at 800 K, and we obtain a similar 0.36 W m^{-1} K^{-1} here. Two separate reports give the κ_{iso} of *Pnma* GeSe to be 2.63 and 1.77 W m^{-1} K^{-1} at 300 K,[13,63] and our calculated value of 2.35 W m^{-1} K^{-1} falls within this range. Our calculated room-temperature $\kappa_{iso} = 4.36$ W m^{-1} K^{-1} for *R*3*m* GeTe is around 30% higher than the experimentally-measured ~3.4 W m^{-1} K^{-1}.[64] The thermal conductivity of *Fm*$\bar{3}$*m* GeTe has been measured as ~1.5 W m^{-1} K^{-1} and predicted to be 0.75–1.25 at 700 K,[27,65] the latter of which compares well to the value of 0.72 W m^{-1} K^{-1} from our calculations. The room-temperature κ_{iso} of *Fm*$\bar{3}$*m* SnTe has been measured between ~2–4.5 W m^{-1} K^{-1} at 300 K,[25,66,67] and our predicted value of 5.01 W m^{-1} K^{-1} is compatible with the upper limit. We note that the variation among the four samples reported in ref. 66 highlights the sensitivity of the measured thermal conductivity to the sample preparation.

Barring two exceptions, the materials can be grouped by structure type. *Cmcm* SnSe has the lowest κ_{iso}, followed by *Pnma* SnTe, GeTe and SnSe, then *Fm*$\bar{3}$*m* GeSe and GeTe, and finally *R*3*m* SnTe and GeTe. *Cmcm* SnSe is therefore predicted to have the smallest κ_{iso} across all ten systems, which is consistent with its exceptional thermoelectric performance.[55,68,69] The two exceptions to the trend are *Pnma* GeSe, which falls between the two lighter *Fm*$\bar{3}$*m* systems and the *R*3*m* systems, and *Fm*$\bar{3}$*m* SnTe. Among the four *Pnma* systems, the ordering in the 300 K thermal conductivity of SnTe < SnSe ≃ GeSe < GeSe largely follows the average masses in Table 2. We therefore do not consider the κ_{iso} of GeSe to be an outlier. The same holds for the two *R*3*m* phases, *i.e.* the κ_{iso} of SnTe is lower than that of GeTe, but with just two data points we cannot really consider this a trend. On the other hand, while *Fm*$\bar{3}$*m* GeSe has a lower κ_{iso} than GeTe, as expected, SnTe, with the largest average mass, has a much larger predicted κ_{iso}, and therefore does represent an outlier here.

It is also of interest to investigate how modes with different frequencies contribute to the $\boldsymbol{\kappa}$. This can be determined from a cumulative sum of the $\boldsymbol{\kappa}_\lambda$ in eqn (2) as a function of frequency at a reference temperature T:

$$\boldsymbol{\kappa}(\omega, T) = \frac{1}{N_{\boldsymbol{q}} V} \sum_{\omega_\lambda \leq \omega} \boldsymbol{\kappa}_\lambda(T) \tag{8}$$

Fig. 5 shows the cumulative κ_{iso} at $T = 300$ K for the four representative systems in Fig. 2, *viz.* *Pnma* GeSe, *R*3*m* GeTe, *Cmcm* SnSe and *Fm*$\bar{3}$*m* SnTe. For *Pnma* GeSe, which has

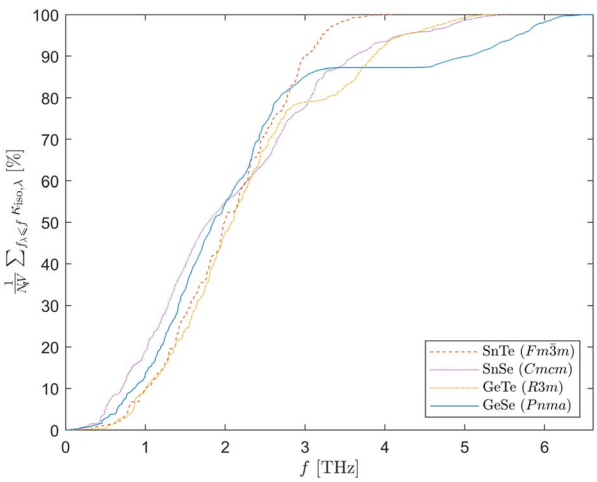

Fig. 5 Cumulative κ_{iso} as a function of frequency at $T = 300$ K for *Pnma* GeSe, *R*3*m* GeTe, *Cmcm* SnSe and *Fm*$\bar{3}$*m* SnTe.

a bandgap in its dispersion (*c.f.* Fig. 2d), around 85% of the thermal conductivity is due to transport through the 50% of the modes below the gap. There is also a clear flattening of the cumulative κ_{iso} over the gap region, as the absence of modes means there is no thermal transport over this frequency range. The cumulative κ_{iso} of *R*3*m* GeTe shows similar behaviour, with a notable reduction in the rate of accumulation around *ca.* 3 THz coinciding with the dip in the DoS (*c.f.* Fig. 2b) and a ~75–80% contribution from the modes below this frequency. While *Cmcm* SnSe does not have a phonon bandgap, if we take the midpoint of the spectrum to be ~3 THz, around 85% of the κ_{iso} is from transport through modes with frequencies below this cutoff, which is consistent with the *Pnma* and *R*3*m* systems. On the other hand, for the heaviest compound, $Fm\bar{3}m$ SnTe, for which the phonon spectrum extends to around 4 THz, around 95% of the thermal conductivity is through modes below ~3 THz. Across all four compounds, therefore, the low-frequency phonon modes with f_λ < 2.5–3 THz contribute > 75% of κ_{iso}. This can be understood based on the fact that the lower-frequency modes tend to have wider dispersions than the higher-frequency modes, resulting in larger group velocities, and are also more heavily populated, *i.e.* have larger occupation numbers n_λ at a given temperature (*c.f.* Fig. 2, eqn (4) and (5)).

3.4 Group velocity *versus* lifetimes

We have previously shown that differences in lattice thermal conductivity can be attributed quantitatively to differences in the phonon group velocities and lifetimes using a constant relaxation-time approximation (CRTA) analysis.[40–42] In this model, we choose a (scalar) temperature-dependent average lifetime τ^{CRTA} such that the $\boldsymbol{\kappa}$ can be written approximately as:

$$\boldsymbol{\kappa}(T) \simeq \frac{1}{N_q V}\tau^{CRTA}(T)\sum_\lambda \frac{\boldsymbol{\kappa}_\lambda(T)}{\tau_\lambda(T)} = \frac{1}{N_q V}\tau^{CRTA}(T)\sum_\lambda C_\lambda(T)\boldsymbol{\nu}_\lambda \otimes \boldsymbol{\nu}_\lambda \quad (9)$$

The term in the summand is calculated from the C_λ and $\boldsymbol{\nu}_\lambda$, both of which are obtained within the harmonic approximation, whereas the τ^{CRTA} are derived from the τ_λ and depend on the anharmonic phonon interactions. Both the harmonic sum $\boldsymbol{\kappa}/\tau^{CRTA}$ and the τ^{CRTA} are normalised such that they are directly comparable between systems in the same way as the macroscopic $\boldsymbol{\kappa}$. The C_λ are a relatively shallow function of the phonon frequency and quickly saturate to the Dulong–Petit limit of $N_A k_B$ per mode at mid-to-high temperature, and thus differences in the harmonic sum largely reflect differences in the $\boldsymbol{\nu}_\lambda$. The τ^{CRTA} are effectively a weighted average over the τ_λ, weighted toward the modes that make the largest contributions to the thermal conductivity. A comparison of the τ^{CRTA} to the frequency spectra of the phonon lifetimes for each of the ten systems at 300 K is provided in Section 3 of the ESI.† Finally, we note that in the formulation in eqn (9) the harmonic sum is a tensor, and an analogous scalar average to κ_{iso}, denoted $(\boldsymbol{\kappa}/\tau^{CRTA})_{iso}$, can be taken for easier comparison between systems.

The $(\boldsymbol{\kappa}/\tau^{CRTA})_{iso}$ as a function of temperature are shown for the ten compounds in Fig. 6a, and the values at 300 K are provided in Table 3. As found in our previous work on the silicon clathrates,[42] we see a strong dependence on the number of atoms n_a in the primitive cell and the crystal symmetry. The four *Pnma* phases, which have the largest $n_a = 8$, have the lowest values, the two *R*3*m* phases have intermediate values ($n_a = 2$, lower symmetry), and the three $Fm\bar{3}m$ phases have the largest values ($n_a = 2$, higher symmetry). The large unit cell of the *Pnma* structure therefore lends itself to lower phonon group velocities, as does the symmetry breaking in the *R*3*m* structure compared to the $Fm\bar{3}m$ phase. *Cmcm* SnSe is an outlier here, as despite its relatively large primitive cell ($n_a = 4$) and low orthorhombic symmetry it has a larger $(\boldsymbol{\kappa}/\tau^{CRTA})_{iso}$ than *R*3*m* GeTe and SnTe and $Fm\bar{3}m$ SnTe. We attribute this to the imaginary modes leading to a sharp dispersion and large $\boldsymbol{\nu}_\lambda$ in some of the phonon branches (*c.f.* Fig. 2c and eqn (5)). In reality, above the *Pnma* → *Cmcm* transition temperature we would

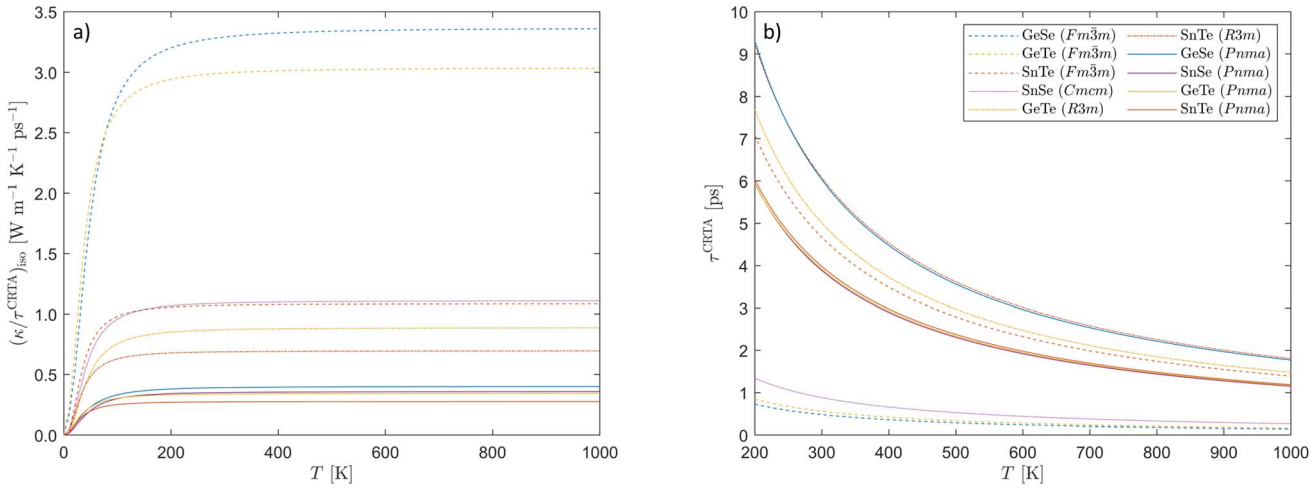

Fig. 6 Constant relaxation-time approximation (CRTA) analysis of the lattice thermal conductivity of the ten chalcogenides examined in this work (eqn (9)): (a) calculated averaged harmonic sum $(\boldsymbol{\kappa}/\tau^{CRTA})_{iso}$ and (b) calculated average lifetimes τ^{CRTA} as a function of temperature.

expect the imaginary modes to be "renormalised" to real frequencies.[33,62] The experiments in ref. 34 noted a substantial phonon softening in SnSe with temperature, leading to a reduction in the $\boldsymbol{\nu}_\lambda$ on the order of 20%, which would not be captured by the fixed-volume structures used in our calculations. It is therefore not clear whether this phenomenon is a feature of materials with soft-mode phase transitions. Finally, for a given crystal structure we observe a clear dependence of the $(\boldsymbol{\kappa}/\tau^{\mathrm{CRTA}})_{\mathrm{iso}}$ on the average mass, such that the values fall in the order of SnTe < SnSe $\simeq$ GeTe < GeSe, SnTe < GeTe, and SnTe $\ll$ GeTe < GeSe for the *Pnma*, *R*3*m* and *Fm*$\bar{3}$*m* phases.

On the other hand, the τ^{CRTA} values do not exhibit any obvious trends (Fig. 6b and Table 3). Three of the four *Pnma* crystal structures, SnSe, GeTe, and SnTe, have very similar averaged phonon lifetimes between 3.89–3.98 ps at 300 K, whereas the τ^{CRTA} of the lighter *Pnma* GeSe is approximately ~50% longer at 6.03 ps. Among the three *Fm*$\bar{3}$*m* structures, both GeSe and GeTe display very short averaged lifetimes of around 0.5 ps, whereas SnTe has a much longer τ^{CRTA} of 4.67 ps that exceeds those of three of the four *Pnma* systems. The two *R*3*m* crystal structures both exhibit consistently longer τ^{CRTA} than other phases with the same chemical composition. Lastly, the τ^{CRTA} of *Cmcm* SnSe is approximately ~25% that of the *Pnma* phase at 300 K. This shorter τ^{CRTA} plays a crucial role in compensating for the roughly threefold increase in the $(\boldsymbol{\kappa}/\tau^{\mathrm{CRTA}})_{\mathrm{iso}}$ term, resulting in an overall lower κ_{iso} compared to the lower-symmetry *Pnma* phase. The variation in the τ^{CRTA} values across the ten systems is thus somewhat intricate, necessitating a more detailed analysis of the underlying physical mechanisms, which is the subject of the following section.

3.5 Anharmonicity *versus* conservation of energy

In the SM-RTA model employed in this work the phonon lifetimes τ_λ are calculated as the inverse of the linewidths Γ_λ. The Γ_λ are determined as twice the imaginary part of the phonon self-energy from a sum of contributions from three-phonon scattering processes according to:[39]

$$\begin{aligned}\Gamma_\lambda(T) = 2\times\frac{18\pi}{\hbar^2}\sum_{\lambda'\lambda''}|\Phi_{-\lambda\lambda'\lambda''}|^2 \\ \times\{[n_{\lambda'}(T)+n_{\lambda''}(T)+1]\delta(\omega_\lambda-\omega_{\lambda'}-\omega_{\lambda''}) \\ +[n_{\lambda'}(T)-n_{\lambda''}(T)][\delta(\omega_\lambda+\omega_{\lambda'}-\omega_{\lambda''})-\delta(\omega_\lambda-\omega_{\lambda'}+\omega_{\lambda''})]\}\end{aligned} \tag{10}$$

Here $\Phi_{\lambda,\lambda',\lambda''}$ are the temperature-independent three-phonon interaction strengths determined perturbatively from the harmonic frequencies and displacement vectors (eigenvectors) and the third-order force constants $\boldsymbol{\Phi}^{(3)}$. These are how phonon anharmonicity is formally introduced in this model. The functions $\delta(x) = 1$ if $x = 0$ and zero otherwise enforce the conservation of energy, while the $\Phi_{\lambda,\lambda',\lambda''}$ contain an analogous function $\Delta(x)$ which enforces conservation of (crystal) momentum.[39] These "selection rules" for the conservation of energy (and also momentum) are a product of the harmonic phonon frequency spectrum, as are the occupation numbers n_λ which also contribute to the scattering probabilities (*c.f.* eqn (4)). A complete description of the method used to calculate the linewidths can be found in ref. 39.

Following ref. 39, we define an approximate linewidth $\tilde{\Gamma}_\lambda$ as:

$$\tilde{\Gamma}_\lambda(T) = 2\times\frac{18\pi}{\hbar^2}P_\lambda N_2(\boldsymbol{q}_\lambda,\omega_\lambda,T) \tag{11}$$

The P_λ are the averaged three-phonon interaction strengths given by:

$$P_\lambda = \frac{1}{(3n_{\mathrm{a}})^2}\sum_{\lambda'\lambda''}\left|\Phi_{\lambda,\lambda',\lambda''}\right|^2 \tag{12}$$

$N_2(\boldsymbol{q}, \omega, T)$ is a weighted two-phonon joint density of states (w-JDoS) function that counts the number of energy- and momentum-conserving scattering pathways available to a phonon with wavevector $\boldsymbol{q}$ and frequency ω and therefore defines the scattering phase space:

$$N_2(\boldsymbol{q},\omega,T) = N_2^{(1)}(\boldsymbol{q},\omega,T) + N_2^{(2)}(\boldsymbol{q},\omega,T) \tag{13}$$

$$\begin{aligned}N_2^{(1)}(\boldsymbol{q},\omega) = \frac{1}{N_{\boldsymbol{q}}}\sum_{\lambda'\lambda''}\Delta(-\boldsymbol{q}+\boldsymbol{q}'+\boldsymbol{q}'')\times \\ [n_{\lambda'}(T)-n_{\lambda''}(T)][\delta(\omega+\omega_{\lambda'}-\omega_{\lambda''})-\delta(\omega-\omega_{\lambda'}+\omega_{\lambda''})]\end{aligned} \tag{14}$$

$$\begin{aligned}N_2^{(2)}(\boldsymbol{q},\omega) = \frac{1}{N_{\boldsymbol{q}}}\sum_{\lambda'\lambda''}\Delta(-\boldsymbol{q}+\boldsymbol{q}'+\boldsymbol{q}'')\times \\ [n_{\lambda'}(T)+n_{\lambda''}(T)+1]\delta(\omega-\omega_{\lambda'}-\omega_{\lambda''})\end{aligned} \tag{15}$$

where as noted above the function $\Delta(x)$ enforces the conservation of crystal momentum. The functions $N_2^{(1)}$ and $N_2^{(2)}$ count separately the number of collision/coalescence (two phonons in, one out; Class 1) and decay/emission pathways (one phonon in, two out; Class 2). It has been noted in previous work that the N_2 can be used to explain the non-smooth variation of the phonon linewidths with respect to frequency and wavevector, with large N_2 tracking broader linewidths and shorter phonon lifetimes.[39]

For comparison between systems, it is useful to average the N_2 over $\boldsymbol{q}$ to obtain functions of frequency only, *i.e.*:

$$\begin{aligned}\overline{N}_2(\omega,T) = \overline{N}_2^{(1)}(\omega,T)+\overline{N}_2^{(2)}(\omega,T) \\ = \frac{1}{N_{\boldsymbol{q}}}\sum_{\boldsymbol{q}}N_2^{(1)}(\boldsymbol{q},\omega,T)+\frac{1}{N_{\boldsymbol{q}}}\sum_{\boldsymbol{q}}N_2^{(2)}(\boldsymbol{q},\omega,T)\end{aligned} \tag{16}$$

We also note that to be comparable between systems with different n_{a} the $N_2/\bar{N}_2$ need to be scaled by a factor of $1/(3n_{\mathrm{a}})^2$, which is folded into the definition of the P_λ in eqn (12).

The calculated $\bar{N}_2{}^{(1)}$ and $\bar{N}_2{}^{(2)}$ of *Cmcm* SnSe at 300 K are shown in Fig. 7, and equivalent plots for all ten systems are provided in Section 4 of the ESI.† In general, collisions are dominant at low frequencies up to around 2 THz, above which phonons have sufficient energy to access decay pathways, and these become competitive with collisions from ~2–3 THz and dominate at higher frequencies. The total number of scattering pathways also generally increases considerably at frequencies approaching the maximum frequency f_{max} in the phonon spectrum. With reference to the cumulative κ_{iso} in Fig. 5, which

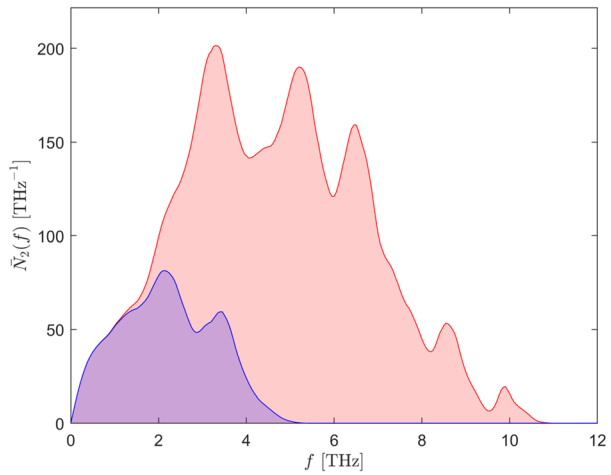

Fig. 7 Averaged two-phonon weighted joint density of states (w-JDoS) $\bar{N}_2(f)$ (eqn (16)) for *Cmcm* SnSe. The separate contributions from collision ($\bar{N}_2^{(1)}$) and decay processes ($\bar{N}_2^{(2)}$) are shown in blue and red, respectively, as a stacked-area plot.

indicate that the majority of the thermal transport occurs through modes with $f_\lambda < 3$ THz, this analysis shows that the averaged lifetimes are limited mainly by collision processes, and, assuming similar interaction strengths, that transport through the higher-energy modes may be limited by a larger scattering phase space.

A comparison of the normalised $\bar{N}_2$ of the ten systems (Fig. 8a) reveals some notable trends. After normalisation the scattering phase space depends strongly on n_a, such that at most frequencies the $\bar{N}_2$ are highest for the *Pnma* phases ($n_a = 8$), intermediate for *Cmcm* SnSe ($n_a = 4$), and lowest and comparable for the *R3m* and *Fm*$\bar{3}$*m* phases ($n_a = 2$). This can be attributed to the more complex phonon spectra enabling more scattering pathways (*c.f.* Fig. 2). Also, the fine structure in the phonon DoS curves is partially reflected in the $\bar{N}_2$, with those of the *Pnma* phases showing a mid-frequency reduction reminiscent of the phonon bandgaps in the DoS. However, whereas the phonon bandgap in *Pnma* GeSe occurs at ~3.5–3 THz, the minimum in the $\bar{N}_2$ occurs around 6 THz, and the absence of modes in the bandgap therefore affects the scattering (largely decay processes) of the high-frequency optic modes. However, the reduction in the DoS of *R3m* GeTe at intermediate frequencies in Fig. 2b does not appear to be reflected in the $\bar{N}_2$, at least not as clearly as in the corresponding *Pnma* phase. Finally, the spread of the $\bar{N}_2$ depends on the spread of the frequency spectra. Among the four *Pnma* phases, the $\bar{N}_2$ of SnTe is notably "compressed" compared to that of GeTe, with larger features at lower frequencies, while SnSe and GeTe have similar $\bar{N}_2$. A crude comparison of the size of the phase space obtained by integrating the $\bar{N}_2$ from zero to the maximum frequency f_{max} in the phonon spectra confirms that a narrower frequency spectrum generally results in a larger scattering phase space (Table 3).

For a more quantitative analysis, we replace the $|\Phi_{-\lambda\lambda'\lambda''}|^2$ in eqn (10) with a constant value $\tilde{P}$ representing a weighted average of the P_λ defined in eqn (12). With this substitution, the κ is inversely proportional to $\tilde{P}$ and a suitable value to reproduce the κ at a given temperature can be determined from a linear fit.[40–42] In the same way as the τ^{CRTA} are a weighted-average lifetime, the $\tilde{P}$ are a weighted average of the $\Phi_{-\lambda\lambda'\lambda''}/P_\lambda$. We note that, like the $N_2/\bar{N}_2$, the $\tilde{P}$ scale with the size of the primitive cell and need to be multiplied by $(3n_a)^2$ to compare between systems. The values of $\tilde{P}$ computed at $T = 300$ K are presented alongside the κ in Table 3. We also show the linear fits performed to determine these parameters, together with a comparison of the $\tilde{P}$ to the frequency spectra of the P_λ, in Section 5 of the ESI.†

Finally, we can combine the averaged lifetimes τ^{CRTA} with the $\tilde{P}$ using eqn (11) to determine a weighted average number of scattering pathways $\tilde{N}_2$ as:

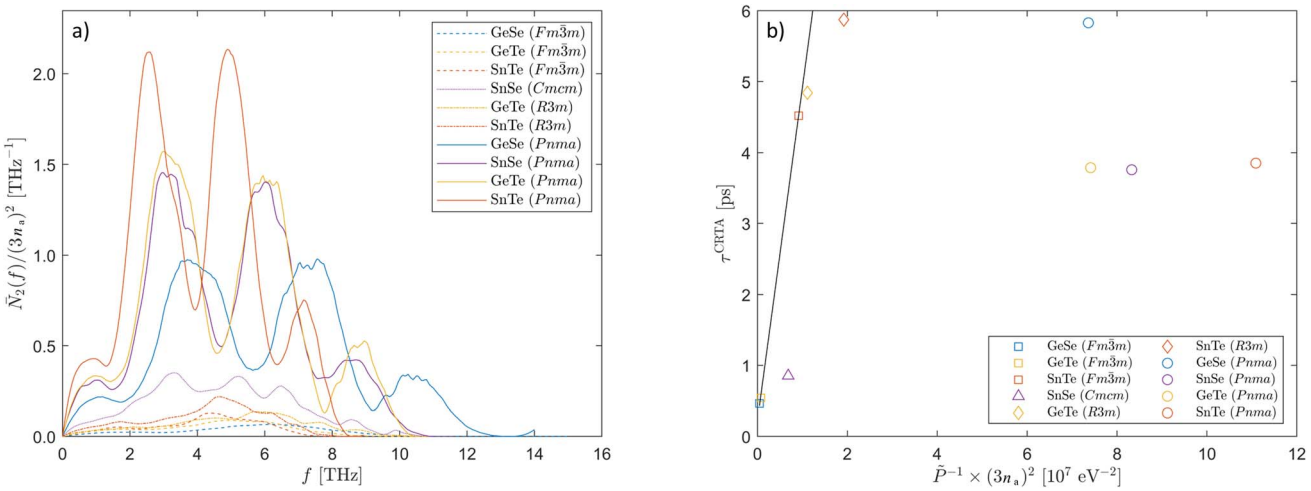

Fig. 8 Analysis of the phonon lifetimes of the ten systems examined in this work. (a) Averaged two-phonon weighted joint density of states (w-JDoS) functions $\bar{N}_2(f)$, defined in eqn (16), for the ten materials examined in this study. The functions have been normalised by $1/(3n_a)^2$ to be comparable between the phases with different n_a. (b) Comparison of the averaged lifetimes τ^{CRTA} and inverse three-phonon interaction strengths $\tilde{P}$ for the ten materials examined in this work at $T = 300$ K. The trendline shows the correlation for the three *Fm*$\bar{3}$*m* systems ($R^2 \approx 1$).

$$\tilde{N}_2 = \frac{\hbar^2}{72\pi^2 \tilde{P} \tau^{\mathrm{CRTA}}} \quad (17)$$

These $\tilde{N}_2$ provide a single value that can be used in conjunction with the qualitative analysis of the $\bar{N}_2$ to assess the impact of differences in the size of the scattering phase space on the phonon linewidths/lifetimes.

This analysis allows us to discuss the τ^{CRTA} in terms of the strength of the interactions between phonons – anharmonicity in this model – and the size of the scattering phase space enabled by the shape of the phonon spectrum. Systems with a short τ^{CRTA} may show strong phonon–phonon interactions (large $\tilde{P}$) and/or a large phase space (large $\tilde{N}_2$). Conversely, systems with long averaged lifetimes could show weak anharmonicity (small $\tilde{P}$) and/or a small phase space (small $\tilde{N}_2$).

The normalised $\tilde{P}$ in Table 3 span two orders of magnitude and show a clear variation with structure type. The four *Pnma* phases have the smallest values, while $Fm\bar{3}m$ GeTe and GeSe have the largest. $Fm\bar{3}m$ SnTe appears to be an outlier with an order of magnitude smaller $\tilde{P}$ than the other two $Fm\bar{3}m$ structures, which accounts for the longer τ^{CRTA} highlighted in the preceding discussion. *R*3*m* GeTe and SnTe, and *Cmcm* SnSe, all have intermediate values.

The inverse of the $\tilde{P}$ are plotted against the averaged lifetimes τ^{CRTA} at 300 K in Fig. 8b. If the differences in the τ^{CRTA} are mainly determined by differences in the interaction strengths, we would expect a good linear correlation.[42] The three $Fm\bar{3}m$ do show a very good linear correlation ($R^2 \approx 1$), which suggests anharmonicity predominantly accounts for the differences in the lifetimes. While it appears that this correlation could be extended to the two *R*3*m* phases and *Cmcm* SnSe, the correlation was found not to be statistically significant when tested. On the other hand, the four *Pnma* phases form a discrete cluster that clearly does not fall on the trendline set by the other six systems. Compared to the other structures, the lifetimes are considerably shorter than would be expected given the weaker $\tilde{P}$, indicating that the lifetimes of the *Pnma* phases are strongly influenced by the size of the scattering phase space.

The $\tilde{N}_2$ vary over approximately an order of magnitude – *i.e.* they show an order of magnitude less variation than the $\tilde{P}$ – and generally in the opposite direction, being largest for the four *Pnma* phases and smallest for the three $Fm\bar{3}m$ phases. Noting again that the majority of the heat transport occurs through the low-frequency modes (*c.f.* Fig. 5), the $\tilde{N}_2$ (and also the τ^{CRTA} and $\tilde{P}$) will be weighted towards these modes, and the trends among compounds with the same structures reflect the impact of the range of the frequency spectra on the $\bar{N}_2$ (*c.f.* Fig. 8a).

Overall, the $\tilde{P}$ span two orders of magnitude and are largest for the more symmetric structures, whereas the $\tilde{N}_2$ span one order of magnitude and are largest for the less symmetric structures. Together, these two competing factors account for the roughly one order of magnitude variation in the τ^{CRTA}. The long τ^{CRTA} of $Fm\bar{3}m$ SnTe and the two *R*3*m* phases highlighted in the previous section can, based on the analysis here, be attributed to a combination of relatively low $\tilde{P}$ and $\tilde{N}_2$, indicative of weak anharmonicity and a small scattering phase space, respectively. Similarly, as noted above, the analysis shows that the weak anharmonicity (low $\tilde{P}$) of the *Pnma* phases is compensated by a large number of scattering pathways (large $\tilde{N}_2$) due to the large primitive cells and relatively complex phonon spectra, and this is why these four systems do not follow the trend in Fig. 8b. Finally, the ~80% shorter averaged lifetime of *Cmcm* SnSe compared to the related *Pnma* phase is a favourable balance of an order of magnitude higher $\tilde{P}$ but a 50% smaller $\tilde{N}_2$.

3.6 Discussion

Our analysis shows that the link between the κ and structure type of the group IV–VI chalcogenides can be explained through two opposing trends.

The first trend is that the complexity of the structure, in particular the number of atoms n_a in the primitive cell, determines the phonon group velocities. To explain this, we consider the "toy model" of a 1D diatomic chain comprising a unit cell of length a with two independent atoms of mass m and two bond force constants k and g (Fig. 9). In this model, the group velocity of the acoustic modes is given analytically by:

$$v_a = a\sqrt{\frac{k \times g}{2m(k+g)}} \quad (18)$$

Taking the case where $k = g = 1$ as our reference point, we introduce bonding inhomogeneity by increasing the difference $\Delta = (k - g)/k$ while maintaining the average $(k + g)/2 = 1$. The v_a is maximised when $k = g$ (homogeneous bonding) and falls to zero at $\Delta = 1$ when phonon propagation is blocked ($g = 0$, *i.e.* one of the two bonds is broken). This simple model therefore demonstrates that irregular chemical bonding can reduce the group velocity. A large primitive cell (large n_a), or, for a given n_a, a spacegroup with fewer symmetry operations, implies fewer

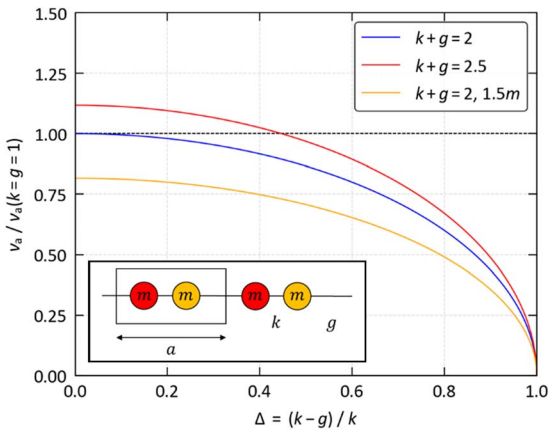

Fig. 9 Group velocities in a 1D diatomic chain with unit-cell length a containing two independent atoms with mass m connected by harmonic spring constants k and g (inset). The three lines compare the relative acoustic-mode group velocity v_a as a function of the difference $\Delta = (k - g)/k$ between $\Delta = 0$ ($k = g$) and $\Delta = 1$ ($g = 0$). The blue line shows the v_a with an average bond strength $(k + g)/2 = 1$, the red line shows the effect of increasing the average bond strength by 25% to $(k + g)/2 = 1.25$, and the orange line shows the effect of increasing the mass by 50% to 1.5 m.

equivalent chemical bonds and therefore less regular bonding, which explains the strong correlation with the group velocities.

For completeness, we also consider the effect of increasing the average bond strength by 25% and increasing the mass by 50%. In the first case, at small Δ the ν_a is larger, as expected, but around $\Delta \sim 0.45$ the group velocity falls below that of the first model with $k = g = 1$. This shows that large bonding inhomogeneity can potentially offset stronger (average) bonding to produce overall lower group velocities. In the second case, the ν_a are simply scaled down by $\sqrt{1.5}$, which shows how increasing the (average) mass also reduces the group velocities.

An important qualitative conclusion is that large average mass and/or weak chemical bonding, which are often taken to be indicators of low lattice thermal conductivity, are secondary to the complexity of the structure. On this point we note that, with the exception of the two *R*3*m* structures, the chalcogenide phases with larger n_a are also in lower-symmetry space groups, so we cannot easily decouple these in our definition of "structural complexity". However, our previous work on the Si clathrates[42] strongly suggests that the n_a rather than the crystal (spacegroup) symmetry is likely to be the key descriptor. Another interesting observation from our analysis is the imaginary modes in *Cmcm* SnSe producing a steep dispersion and larger $\boldsymbol{\nu}_\lambda$ compared to the *Pnma* phase. The impact of anharmonic renormalisation and potential phonon softening at elevated temperature[34] on this behaviour requires further investigation.

The second trend is that the crystal symmetry has a strong bearing on the phonon lifetimes through opposing effects on the anharmonic three-phonon interaction strengths and the size of the scattering phase space.

We propose a structural basis for the differences in interaction strengths based on the revised lone-pair model of Walsh *et al.*[70] In the IV–VI monochalcogenides, the tetrel atoms adopt the +2 oxidation state with a valence ns^2 lone pair of electrons. The lone pair is not chemically inert and interacts with the anion p orbitals to form bonding and antibonding states. When this interaction is strong, and the antibonding states have substantial cation s character, the antibonding states can mix with the vacant cation p states through on-site hybridisation, resulting in further stabilisation. The interaction is forbidden by symmetry in a centrosymmetric environment, and therefore drives the tetrel atoms toward distorted, low-coordinate geometries in which an "active" lone pair effectively occupies a coordination site and is often projected into a structural void such as the interlayer space in the *Pnma* and *Cmcm* structures (*c.f.* Fig. 1). When the tetrel atoms are constrained to a symmetric environment, the lone pair is "strained", which can provide a driving force for anharmonic lattice dynamics. In the extreme, this manifests as imaginary harmonic modes, for example in *Cmcm* SnSe, as shown in the present work (*c.f.* Fig. 2c and 3), but also in the $Fm\bar{3}m$ and *Cmcm* phases of SnS[60] and the $Fm\bar{3}m$ phase of GeSe. Competing with this, however, is the potential energetic destabilisation associated with the lower coordination number, and if the interaction between the cation s and anion p states is weak the stabilisation from an active lone pair does not outweigh the reduction in coordination number and a symmetric structure is energetically preferred. In the PbX series, PbO adopts the distorted litharge structure with an active lone pair, whereas the lead chalcogenides PbS, PbSe and PbTe adopt the centrosymmetric rocksalt structure without an active lone pair.[70] Similarly, the strong anion/cation interaction in SnS results in an energetic preference for the *Pnma* structure and the $Fm\bar{3}m$ structure being dynamically unstable, whereas the weaker interaction in SnSe results in the rocksalt phase being both dynamically stable and much closer to the convex hull.[60]

In the SM-RTA model used in these calculations, strong three-phonon interactions arise from a large response of the system to atomic displacements at third order. It has been demonstrated that the electron-phonon coupling due to the lone-pair activity in *Cmcm* SnSe contributes directly to large third-order force constants and strong phonon–phonon interactions.[34] Similarly, although the Pb chalcogenides are stable in the rocksalt phase, indicating, in principle, weaker electron-phonon coupling, PbTe has been characterised as an "incipient ferroelectric",[71] which could also be driven by lone pair activity and which has been linked to strong scattering and suppressed heat transport through the longitudinal acoustic (LA) modes.[18] Similarly, while in principle the interaction between Ge and S/Se might be expected to be too weak to drive a structural distortion, both materials readily form in the *Pnma* structure, and the presence of active lone pairs has been confirmed both experimentally and theoretically.[72] In our view, these observations provide evidence that lone pair activity could support strong three-phonon interactions across all of the IV–VI chalcogenides, even in systems where the electron-phonon coupling is not strong enough to manifest in the second-order force constants as imaginary harmonic modes.

This mechanism explains the strong link between the crystal symmetry and the phonon interaction strengths. In the $Fm\bar{3}m$ structure the tetrel atoms are forced by symmetry to adopt a centrosymmetric environment, resulting in a "strained" lone pair and strong three-phonon interactions reflected in large $\tilde{P}$. In the *Pnma* structure, on the other hand, the tetrel atoms can adopt a distorted local geometry with active lone pairs projecting into the interlayer space, leading to weak three-phonon interactions and low $\tilde{P}$. In the *R*3*m* structure, the tetrel atoms are in a less symmetric environment than in the $Fm\bar{3}m$ phase, allowing for some relaxation of the strain, but not as much as in the *Pnma* phase. Similarly, in the *Cmcm* structure the tetrel atoms are forced to adopt a more symmetric environment than in the *Pnma* phase, which leads to larger three-phonon interactions. Both of these systems therefore have $\tilde{P}$ intermediate between the bounds set by the (fully) symmetric $Fm\bar{3}m$ and (fully) distorted *Pnma* phases. Finally, the strength of the electronic interactions is determined by the energy match between the cation s and anion p states, and this can potentially explain the variation in anharmonicity among different compounds in the same structure type, although to explore this further would require a detailed analysis of the atomic energy levels and the chemical bonding in the different chalcogenide systems.[70]

Finally, our analysis of the averaged lifetimes shows that the three-phonon interaction strengths and anharmonicity, as defined by the $\tilde{P}$, are not the only important factor, and that the reduced anharmonicity of the lower-symmetry crystal structures is partially offset by the more complex phonon spectra facilitating a larger scattering phase space. Our analysis suggests that this plays a particularly important role in determining the low κ of the *Pnma* structures.

Table 4 summarises qualitatively the factors that determine the κ across the four chalcogenide phases examined in this work. Given that low group velocities are favoured by inhomogeneous bonding typical of large unit cells and low-symmetry structures, whereas strong anharmonicity is favoured by symmetric tetrel environments typical of high-symmetry structures, the κ is in principle a balance of two competing trends. However, some chalcogenide structure types appear to "decouple" these factors. The *Cmcm* phase is a low-symmetry structure, but the tetrel atoms are confined to locally-symmetric environments, resulting in an optimal trade-off between relatively low group velocities and strong anharmonicity. The recently-discovered π-cubic structure, reported as a synthetically-accessible phase of SnS and SnSe,[73,74] has a high-symmetry cubic $P2_13$ spacegroup but a complex structure with $n_a = 64$ atoms in the primitive cell that allows the tetrel atoms to adopt distorted local geometries similar to the *Pnma* phase. Based on our findings we would anticipate ultra-low group velocities compensating for weak anharmonicity, representing perhaps the other "extreme" to the *Cmcm* phase. Exploring crystal-engineering routes to obtain the IV–VI chalcogenides in different crystal phases is therefore likely to be a fruitful avenue for optimising the lattice thermal conductivity for thermoelectric applications.

Another potential avenue would be to try to optimise the κ of the rocksalt systems by reducing the group velocities while retaining the strong intrinsic anharmonicity. Experimental studies have demonstrated that solid solutions of *Pnma* SnS and SnSe can display lower κ than both endpoints,[75–78] and our recent modelling suggests this is primarily due to a reduction in the ν_λ,[41] so alloying may be a facile route to achieving this. Another possibility is the "discordant doping" approach demonstrated by Xie *et al.*[79] where a carefully-selected dopant is incorporated into the lattice at a few at% to deliberately induce structural distortion and chemical bond strain. Based on the analysis presented here, we would expect this to also lead to a reduction in the group velocities, and to thus be a viable strategy to lower the κ of rocksalt-structured chalcogenides.

More generally, the links between the group velocities and the size of the scattering phase space, and the structural complexity, are likely to be "universal", with the caveat that stronger bonding and/or lighter elements will result in a larger range of phonon frequencies, and, consequently, larger group velocities and potentially a smaller scattering phase space. On the other hand, the link between the phonon interaction strengths and the local coordination environment of the tetrel atoms will be specific to compounds including species that can show stereochemically active lone pairs, such as IV(II) and V(III) ions. We would therefore expect this to generalize to Group IV oxides and perhaps to Group V sesquioxides and sesquichalcogenides, but it is unlikely to be universal. It is noteworthy, however, that strain induced by local symmetry has also been proposed as a factor in the low lattice thermal conductivity of $CuFe_{1-x}Ge_xS_2$,[80] $AgInSe_2$ (ref. 81) and $Cu_{1-x}Ag_xGaTe_2$, suggesting there may be a more general principle.[82]

Finally, we also discuss the key approximations in our methodology. First of all, we determine the κ within the SM-RTA, as opposed to solving the linearised phonon Boltzmann transport equation (LBTE). To test the impact of this, we calculated the κ of the ten materials by solving the LBTE and compared the results to the RTA calculations (see Section 6 of the ESI†). The LBTE solution results in a significant increase in the predicted room-temperature κ of the $Fm\bar{3}m$ systems, of 75 and 80% for GeSe and GeTe, respectively, and 28% for SnTe. The LBTE also has a smaller but significant impact on the two $R3m$ phases and *Cmcm* SnSe, increasing the κ by 11/12 and 22%, respectively. The impact on the *Pnma* phases is smallest, increasing the κ by between 0.3% for *Pnma* SnSe and 7% for *Pnma* SnTe. Interestingly, the size of the difference appears to correlate well with the $\tilde{P}$, such that compounds with stronger phonon–phonon interactions in this definition show a larger increase in κ from solving the LBTE over using the simpler RTA method. Given that solving the LBTE entails diagonalising collision matrices, which depend on the interaction strengths, this is perhaps not surprising.

Secondly, the method uses the ν_λ and C_λ calculated within the harmonic approximation, and linewidths and lifetimes are determined from perturbative anharmonicity at third order, both using force constants calculated for the (athermal) equilibrium lattice volume. In reality, we would expect some temperature renormalisation of the phonon spectrum, as discussed above for *Cmcm* SnSe, and we might also expect a contribution to the phonon linewidths from higher-order (*e.g.* 4^{th}-order) scattering processes. A variety of techniques exist for

Table 4 Summary of the factors affecting the lattice thermal conductivity of the four Group IV–VI chalcogenide structure types examined in this study

	Bonding	Tetrel environment	Group velocities	Lifetimes	Interaction strengths	Phase space
$Fm\bar{3}m$	Homogeneous	Most constrained	Large	Shortest	Strongest	Small
$R3m$	<$Fm\bar{3}m$	Intermediate	Medium	Longest	Weak	Small
Cmcm	<$R3m$	Intermediate	Medium	Short	Strong	Medium
Pnma	Least homogeneous	Least constrained	Small	Long	Weakest	Large

modelling the temperature renormalisation of the phonon spectrum, including the decoupled anharmonic mode approximation (DAMA)[83] and temperature-dependent effective potential (TDEP) methods[84] and the stochastic self-consistent harmonic approximation (SSCHA).[85] We previously found that using a simple approach, similar to the DAMA method, to renormalise the soft modes in *Cmcm* SnSe had a minimal impact on the calculated κ,[33] whereas the more sophisticated SSCHA approach, including non-perturbative anharmonicity at third order, indicated a much larger impact.[62] A recent study also highlighted a significant impact of fourth-order anharmonicity on the κ of *Cmcm* SnSe.[86] Furthermore, the study in ref. 34 found evidence for strong temperature renormalisation in *Pnma* SnSe, which does not have imaginary harmonic modes.

Accounting for temperature renormalisation of the harmonic phonon spectrum and/or higher-order phonon interactions would, however, significantly increase the cost of the calculations, to the point where a comparative study of a large number of materials, as in the present work, would be impractical. On this point, a recent study on BaXYF (X = Cu, Ag, Y = Se, Te) found that the SM-RTA model may benefit from a favourable cancellation of errors, such that more sophisticated calculations need to include both effects to obtain accurate results.[87] We note that this may explain why our predicted κ are generally a good match to experimental measurements despite the approximations inherent to the method.

Finally, it has been proposed that the quasiparticle description of phonons breaks down, and full-spectrum renormalisation approaches are required, when the anharmonicity is sufficiently strong that the lifetimes fall below the so-called Ioffe–Regel limit in time of $1/(2\pi f_\lambda)$.[88] We therefore compared the spectra of τ_λ for each of the ten systems at our chosen analysis temperature of 300 K to this limit, and found that, in all cases, the lifetimes were above it, indicating that the quasiparticle description should be reasonable (see Section 7 of the ESI†). However, we observe a similar trend to comparing the RTA and LBTE κ, whereby the spectra of τ_λ for the systems with larger averaged interaction strengths are closer to the Ioffe–Regel limit. This suggests that, despite the approximations inherent in calculating them, the $\tilde{P}$ are a reasonable qualitative descriptor of anharmonicity.

An important point is that more sophisticated theoretical treatments would complicate the data analysis and make extracting chemical insight much more challenging. The key question, then, is whether the RTA calculations are sufficiently accurate to capture the qualitative links between crystal structure and thermal conductivity. The fact that our analysis is consistent with previous theories for the low κ of various IV–VI chalcogenides suggests this most likely is the case. We therefore believe the present study should serve as a useful baseline against which to establish the impact of more intricate physics and chemistry on the thermal conductivity of these materials.

4 Conclusions

In summary, we have performed a detailed microscopic analysis of the lattice thermal conductivity of ten Group IV–VI chalcogenides within the single-mode relaxation-time approximation. Using the constant relaxation-time model, we find that the phonon group velocities are strongly related to the homogeneity in the chemical bonding, captured by the size and symmetry of the primitive unit cell, with a secondary dependence on the atomic masses of the constituent elements. The phonon lifetimes depend more intricately on the structure type and composition through a balance of the intrinsic anharmonicity, maximised in structures that force the tetrel atoms to adopt symmetric local environments, and the size of the scattering phase space, maximised by low-symmetry structures with complex phonon spectra. These effects are best balanced in the high-temperature *Cmcm* phase of SnSe, which shows the lowest κ_{latt} of the ten systems examined, accounting for its ultra-low thermal conductivity and exceptional thermoelectric performance.

Our analysis provides some clear guidance for optimising the thermal transport in the Group IV–VI chalcogenides. If low κ_{latt} is desired, as for thermoelectric applications, a structure with a large and/or low-symmetry unit cell in which the tetrel atoms are constrained to a locally-symmetric environment should be sought. While seemingly contradictory, these requirements appear to be met in the *Cmcm* phase, which is accessible to some of the chalcogenides at high temperature and/or under pressure.[60] Alternatively, it might be possible to use alloying or doping to stabilise the chalcogenide in a rocksalt or *R*3*m* phase while reducing the group velocities. If, on the other hand, high κ_{latt} is required, as might be the case *e.g.* for power electronics, a relatively simple structure in which the tetrel atom can adopt a low-coordinate geometry with an active lone pair should be sought. We note also that while we have focused on (tetrel) selenides and tellurides in this work, it is likely that the same considerations would apply to the analogous Group VI oxides, and possibly more generally *e.g.* to Group V sesquichalcogenides (and sesquioxides).

This study also suggests a number of avenues for future computational studies. Firstly, analysis of the π-cubic phases of *e.g.* SnS and SnSe would confirm, or otherwise, that: (1) the size of the primitive cell, rather than the crystal symmetry, is the key predictor of low group velocities; and (2) that the local environment of the tetrel atoms, rather than the "global" crystal symmetry, is the key predictor of anharmonicity. Secondly, extension of this study to GeS and SnS, and to the Pb chalcogenides PbS, PbSe and PbTe, would provide a more complete picture of the role of the chalcogen and tetrel in defining the κ_{latt}, and would also complement previous studies with new insight into the anharmonicity in the Pb chalcogenides. We aim to address both points in the near future.

Data availability

Raw data from this study, including optimised structures and input and output files from the phonon and lattice-thermal conductivity calculations, will be made available to download free of charge in an online repository at **https://doi.org/10.17632/tkzvj899bx**.

Author contributions

Conceptualisation: JMS; data curation: SKG; formal analysis: JMS and SKG; funding acquisition: JMS, AS and NK; investigation: SKG and JMS; methodology: SKG and JMS; project administration: JMS and AS; supervision: JMS and AS; writing – original draft: SKG; writing – review and editing: all authors.

Conflicts of interest

There are no conflicts to declare.

Acknowledgements

The authors acknowledge helpful discussions with Dr L. Whalley, Dr J. Buckeridge and Dr A. A. Sokol. SKG is supported by the A*STAR PhD programme. JMS is supported by a UK Research and Innovation (UKRI) Future Leaders Fellowship (MR/T043121/1) and previously held a University of Manchester (UoM) Presidential Fellowship. AS acknowledges funding from the A*STAR Career Development Fund (CDF; C210112022). The majority of these calculations were performed on the UK national ARCHER 2 high-performance computing facility *via* JMS's membership of the UK Materials Chemistry Consortium (MCC), which is funded by the UK Engineering and Physical Sciences Research Council (EPSRC; EP/R029431 and EP/X035859). A subset of the calculations and analysis were performed on the UoM Computational Shared Facility, which is maintained by UoM Research IT.

Notes and references

1 *Clean Energy for all Europeans Package, European Commission Rreport*, 2019.
2 *Amending Directive on Energy Efficiency, European Commission Report 2018/844/EU*, 2018.
3 *Energy Performance of Buildings Directive, European Commission Report EU 2018/844*, 2018.
4 IEA, *Meeting Climate Change Goals through Energy Efficiency*, 2017.
5 R. Freer and A. V. Powell, *J. Mater. Chem. C*, 2020, **8**, 441–463.
6 A. Firth, B. Zhang and A. Yang, *Appl. Energy*, 2019, **235**, 1314–1334.
7 C. Cazorla, *Novel Mechanocaloric Materials for Solid-State Cooling Applications*, 2019.
8 G. Bennett, J. Lombardo, R. Hemler, G. Silverman, C. Whitmore, W. Amos, E. Johnson, A. Schock, R. Zocher, T. Keenan, J. Hagan and R. Englehart, in *Mission of Daring: the General-Purpose Heat Source Radioisotope Thermoelectric Generator*, American Institute of Aeronautics and Astronautics, 2006.
9 H. Jaber, M. Khaled, T. Lemenand, R. Murr, J. Faraj and M. Ramadan, *Energy*, 2019, **170**, 1036–1050.
10 G. Tan, L.-D. Zhao and M. Kanatzidis, *Chem. Rev.*, 2016, **116**, 12123–12149.
11 W. G. Zeier, A. Zevalkink, Z. M. Gibbs, G. Hautier, M. G. Kanatzidis and G. J. Snyder, *Angew Chem. Int. Ed. Engl.*, 2016, **55**, 6826–6841.
12 Z. Li, C. Xiao and Y. Xie, *Applied Physics Reviews*, 2022, **9**, 011303.
13 T. Lyu, X. Li, Q. Yang, J. Cheng, Y. Zhang, C. Zhang, F. Liu, J. Li, W. Ao, H. Xie and L. Hu, *Chem. Eng. J.*, 2022, **442**, 136332.
14 K. Manibalan, M. Y. Ho, Y. C. Du, H. W. Chen and H. J. Wu, *Materials*, 2023, **16**, 509.
15 X. Y. Tan, J.-F. Dong, N. Jia, H.-X. Zhang, R. Ji, A. Suwardi, Z.-L. Li, Q. Zhu, J.-W. Xu and Q.-Y. Yan, *Rare Met.*, 2022, 3027–3034.
16 K. Biswas, J. He, I. D. Blum, C.-I. Wu, T. P. Hogan, D. N. Seidman, V. P. Dravid and M. G. Kanatzidis, *Nature*, 2012, **489**, 414–418.
17 C. Guo, D. Wang, X. Zhang and L.-D. Zhao, *Chem. Mater.*, 2022, **34**, 3423–3429.
18 O. Delaire, J. Ma, K. Marty, A. F. May, M. A. McGuire, M.-H. Du, D. J. Singh, A. Podlesnyak, G. Ehlers, M. D. Lumsden and B. C. Sales, *Nat. Mater.*, 2011, **10**, 614–619.
19 Z. M. Gibbs, H. Kim, H. Wang, R. L. White, F. Drymiotis, M. Kaviany and G. Jeffrey Snyder, *Appl. Phys. Lett.*, 2013, **103**, 262109.
20 E. S. Božin, C. D. Malliakas, P. Souvatzis, T. Proffen, N. A. Spaldin, M. G. Kanatzidis and S. J. L. Billinge, *Science*, 2010, **330**, 1660–1663.
21 S. Kastbjerg, N. Bindzus, M. Søndergaard, S. Johnsen, N. Lock, M. Christensen, M. Takata, M. A. Spackman and B. Brummerstedt Iversen, *Adv. Funct. Mater.*, 2013, **23**, 5477–5483.
22 T. Keiber, F. Bridges and B. C. Sales, *Phys. Rev. Lett.*, 2013, **111**, 095504.
23 K. S. Knight, *J. Phys.: Condens. Matter*, 2014, **26**, 385403.
24 A. Feltrin and A. Freundlich, *Renewable Energy*, 2008, **33**, 180–185.
25 R. Moshwan, L. Yang, J. Zou and Z. Chen, *Adv. Funct. Mater.*, 2017, **27**, 1703278.
26 J. Cao, S. W. Chien, X. Y. Tan, C. K. I. Tan, Q. Zhu, J. Wu, X. Wang, Y. Zhao, L. Yang, Q. Yan, H. Liu, J. Xu and A. Suwardi, *ChemNanoMat*, 2021, **7**, 476–482.
27 S. Perumal, M. Samanta, T. Ghosh, U. S. Shenoy, A. K. Bohra, S. Bhattacharya, A. Singh, U. V. Waghmare and K. Biswas, *Joule*, 2019, **3**, 2565–2580.
28 H. Zhang, S. D. Cheng, L. Lu and S. B. Mi, *Nanoscale*, 2021, **13**, 15205–15209.
29 J. Li, Y. Pan, C. Wu, F. Sun and T. Wei, *Sci. China: Technol. Sci.*, 2017, **60**, 1347–1364.
30 M. Samanta, T. Ghosh, R. Arora, U. V. Waghmare and K. Biswas, *J. Am. Chem. Soc.*, 2019, **141**, 19505–19512.
31 Z. Liu, N. Sato, Q. Guo, W. Gao and T. Mori, *NPG Asia Mater.*, 2020, **12**, 66.
32 L.-D. Zhao, S.-H. Lo, Y. Zhang, H. Sun, G. Tan, C. Uher, C. Wolverton, V. P. Dravid and M. G. Kanatzidis, *Nature*, 2014, **508**, 373–377.

33 J. M. Skelton, L. A. Burton, S. C. Parker, A. Walsh, C.-E. Kim, A. Soon, J. Buckeridge, A. A. Sokol, C. R. A. Catlow, A. Togo and I. Tanaka, *Phys. Rev. Lett.*, 2016, **117**, 075502.
34 C. W. Li, J. Hong, A. F. May, D. Bansal, S. Chi, T. Hong, G. Ehlers and O. Delaire, *Nat. Phys.*, 2015, **11**, 1063–1069.
35 S. Li, L. Yin, Y. Liu, X. Wang, C. Chen and Q. Zhang, *J. Mater. Sci. Technol.*, 2023, **143**, 234–241.
36 J. A. Kafalas and A. N. Mariano, *Science*, 1964, **143**, 952.
37 H. Yu and Y. Chen, *J. Phys. Chem. C*, 2018, **122**, 15673–15677.
38 W. Li, J. Carrete, N. A. Katcho and N. Mingo, *Comput. Phys. Commun.*, 2014, **185**, 1747–1758.
39 A. Togo, L. Chaput and I. Tanaka, *Phys. Rev. B: Condens. Matter Mater. Phys.*, 2015, **91**, 094306.
40 J. Tang and J. M. Skelton, *J. Phys.: Condens. Matter*, 2021, 164002.
41 J. M. Skelton, *J. Mater. Chem. C*, 2021, **9**, 11772–11787.
42 B. Wei, J. M. Flitcroft and J. M. Skelton, *Structural Dynamics, Phonon Spectra and Thermal Transport in the Silicon Clathrates*, 2022.
43 G. Kresse and J. Hafner, *Phys. Rev. B: Condens. Matter Mater. Phys.*, 1993, **47**, 558–561.
44 A. Jain, S. P. Ong, G. Hautier, W. Chen, W. D. Richards, S. Dacek, S. Cholia, D. Gunter, D. Skinner, G. Ceder and K. A. Persson, *APL Mater.*, 2013, **1**, 011002.
45 J. P. Perdew, A. Ruzsinszky, G. I. Csonka, O. A. Vydrov, G. E. Scuseria, L. A. Constantin, X. Zhou and K. Burke, *Phys. Rev. Lett.*, 2008, **100**, 136406.
46 S. L. Dudarev, G. A. Botton, S. Y. Savrasov, C. J. Humphreys and A. P. Sutton, *Phys. Rev. B: Condens. Matter Mater. Phys.*, 1998, **57**, 1505–1509.
47 G. Kresse and D. Joubert, *Phys. Rev. B: Condens. Matter Mater. Phys.*, 1999, **59**, 1758–1775.
48 P. E. Blöchl, *Phys. Rev. B: Condens. Matter Mater. Phys.*, 1994, **50**, 17953–17979.
49 A. Togo and I. Tanaka, *Scr. Mater.*, 2015, **108**, 1–5.
50 H. Wiedemeier and P. A. Siemers, *Z. Anorg. Allg. Chem.*, 1975, **411**, 90–96.
51 P. A. E. Murgatroyd, M. J. Smiles, C. N. Savory, T. P. Shalvey, J. E. N. Swallow, N. Fleck, C. M. Robertson, F. Jäckel, J. Alaria, J. D. Major, D. O. Scanlon and T. D. Veal, *Chem. Mater.*, 2020, **32**, 3245–3253.
52 M. G. Herrmann, R. P. Stoffel, M. Kupers, M. Ait Haddouch, A. Eich, K. Glazyrin, A. Grzechnik, R. Dronskowski and K. Friese, *Acta Crystallogr., Sect. B: Struct. Sci., Cryst. Eng. Mater.*, 2019, **75**, 246–256.
53 P. Wu, Y. Ishikawa, M. Hagihala, S. Lee, K. Peng, G. Wang, S. Torii and T. Kamiyama, *Phys. B*, 2018, **551**, 64–68.
54 M. Sist, J. Zhang and B. Brummerstedt Iversen, *Acta Crystallogr., Sect. B: Struct. Sci., Cryst. Eng. Mater.*, 2016, **72**, 310–316.
55 L.-D. Zhao, S.-H. Lo, Y. Zhang, H. Sun, G. Tan, C. Uher, C. Wolverton, V. P. Dravid and M. G. Kanatzidis, *Nature*, 2014, **508**, 373–377.
56 K. Momma and F. Izumi, *J. Appl. Crystallogr.*, 2011, **44**, 1272–1276.
57 L. Shelimova, N. K. Abrikosov and V. Zhdanova, *Zh. Neorg. Khim.*, 1965, **10**, 1200–1205.
58 S. Karbanov, V. Zlomanov and A. Novoselova, *Dokl. Akad. Nauk SSSR*, 1968, **182**, 862–863.
59 P. Bauer Pereira, I. Sergueev, S. Gorsse, J. Dadda, E. Müller and R. P. Hermann, *Phys. Status Solidi B*, 2013, **250**, 1300–1307.
60 I. Pallikara and J. M. Skelton, *Phys. Chem. Chem. Phys.*, 2021, **23**, 19219–19236.
61 M. T. Dove, *Am. Mineral.*, 1997, **82**, 213–244.
62 U. Aseginolaza, R. Bianco, L. Monacelli, L. Paulatto, M. Calandra, F. Mauri, A. Bergara and I. Errea, *Phys. Rev. Lett.*, 2019, **122**, 075901.
63 K. Yuan, Z. Sun, X. Zhang and D. Tang, *Sci. Rep.*, 2019, **9**, 9490.
64 Z. Zheng, X. Su, R. Deng, C. Stoumpos, H. Xie, W. Liu, Y. Yan, S. Hao, C. Uher, C. Wolverton, M. G. Kanatzidis and X. Tang, *J. Am. Chem. Soc.*, 2018, **140**, 2673–2686.
65 M. Ghim, Y.-J. Choi and S.-H. Jhi, *Phys. Rev. B*, 2023, **107**, 184301.
66 D. H. Damon, *J. Appl. Phys.*, 2004, **37**, 3181–3190.
67 S. K. Kihoi, U. S. Shenoy, J. N. Kahiu, H. Kim, D. K. Bhat and H. S. Lee, *ACS Sustain. Chem. Eng.*, 2022, **10**, 1367–1372.
68 L.-D. Zhao, G. Tan, S. Hao, J. He, Y. Pei, H. Chi, H. Wang, S. Gong, H. Xu, V. P. Dravid, C. Uher, G. J. Snyder, C. Wolverton and M. G. Kanatzidis, *Science*, 2016, **351**, 141–144.
69 C. Zhou, Y. K. Lee, Y. Yu, S. Byun, Z.-Z. Luo, H. Lee, B. Ge, Y.-L. Lee, X. Chen, J. Y. Lee, O. Cojocaru-Mirédin, H. Chang, J. Im, S.-P. Cho, M. Wuttig, V. P. Dravid, M. G. Kanatzidis and I. Chung, *Nat. Mater.*, 2021, **20**, 1378–1384.
70 A. Walsh, D. J. Payne, R. G. Egdell and G. W. Watson, *Chem. Soc. Rev.*, 2011, **40**, 4455–4463.
71 R. T. Bate, D. L. Carter and J. S. Wrobel, *Phys. Rev. Lett.*, 1970, **25**, 159–162.
72 M. J. Smiles, J. M. Skelton, H. Shiel, L. A. H. Jones, J. E. N. Swallow, H. J. Edwards, P. A. E. Murgatroyd, T. J. Featherstone, P. K. Thakur, T.-L. Lee, V. R. Dhanak and T. D. Veal, *J. Mater. Chem. A*, 2021, **9**, 22440–22452.
73 R. E. Abutbul, A. R. Garcia-Angelmo, Z. Burshtein, M. T. S. Nair, P. K. Nair and Y. Golan, *CrystEngComm*, 2016, **18**, 5188–5194.
74 R. E. Abutbul, E. Segev, S. Samuha, L. Zeiri, V. Ezersky, G. Makov and Y. Golan, *CrystEngComm*, 2016, **18**, 1918–1923.
75 Y.-M. Han, J. Zhao, M. Zhou, X.-X. Jiang, H.-Q. Leng and L.-F. Li, *J. Mater. Chem. A*, 2015, **3**, 4555–4559.
76 C.-C. Lin, R. Lydia, J. H. Yun, H. S. Lee and J. S. Rhyee, *Chem. Mater.*, 2017, **29**, 5344–5352.
77 Asfandiyar, T.-R. Wei, Z. Li, F.-H. Sun, Y. Pan, C.-F. Wu, M. U. Farooq, H. Tang, F. Li, B. Li and J.-F. Li, *Sci. Rep.*, 2017, **7**, 43262.
78 W. He, D. Wang, H. Wu, Y. Xiao, Y. Zhang, D. He, Y. Feng, Y.-J. Hao, J.-F. Dong, R. Chetty, L. Hao, D. Chen, J. Qin, Q. Yang, X. Li, J.-M. Song, Y. Zhu, W. Xu, C. Niu, X. Li, G. Wang, C. Liu, M. Ohta, S. J. Pennycook, J. He, J.-F. Li and L.-D. Zhao, *Science*, 2019, **365**, 1418–1424.

79 H. Xie, X. Su, S. Hao, C. Zhang, Z. Zhang, W. Liu, Y. Yan, C. Wolverton, X. Tang and M. G. Kanatzidis, *J. Am. Chem. Soc.*, 2019, **141**, 18900–18909.
80 S. Tippireddy, F. Azough, Vikram, A. Bhui, P. Chater, D. Kepaptsoglou, Q. Ramasse, R. Freer, R. Grau-Crespo, K. Biswas, P. Vaqueiro and A. V. Powell, *J. Mater. Chem. A*, 2022, **10**, 23874–23885.
81 Y. Zhu, B. Wei, J. Liu, N. Z. Koocher, Y. Li, L. Hu, W. He, G. Deng, W. Xu, X. Wang, J. M. Rondinelli, L.-D. Zhao, G. J. Snyder and J. Hong, *Mater. Today Phys.*, 2021, **19**, 100428.
82 H. Xie, Z. Li, Y. Liu, Y. Zhang, C. Uher, V. P. Dravid, C. Wolverton and M. G. Kanatzidis, *J. Am. Chem. Soc.*, 2023, **145**, 3211–3220.
83 D. J. Adams and D. Passerone, *J. Phys.: Condens. Matter*, 2016, **28**, 305401.
84 O. Hellman, P. Steneteg, I. A. Abrikosov and S. I. Simak, *Phys. Rev. B: Condens. Matter Mater. Phys.*, 2013, **87**, 104111.
85 L. Monacelli, R. Bianco, M. Cherubini, M. Calandra, I. Errea and F. Mauri, *J. Phys.: Condens. Matter*, 2021, **33**, 363001.
86 J. Sun, C. Zhang, Z. Yang, Y. Shen, M. Hu and Q. Wang, *ACS Appl. Mater. Interfaces*, 2022, **14**, 11493–11499.
87 T. Yue, Y. Zhao, J. Ni, S. Meng and Z. Dai, *Phys. Rev. B*, 2023, **107**, 024301.
88 M. Simoncelli, N. Marzari and F. Mauri, *Phys. Rev. X*, 2022, **12**, 041011.